Lensing is low: cosmology, galaxy formation or new physics?

Alexie Leauthaud,[1,2]⋆ Shun Saito,[3] Stefan Hilbert,[4,5] Alexandre Barreira,[3]
Surhud More,[2] Martin White,[6] Shadab Alam,[7,8] Peter Behroozi,[6]† Kevin Bundy,[1,2]
Jean Coupon,[9] Thomas Erben,[10] Catherine Heymans,[8] Hendrik Hildebrandt,[10]
Rachel Mandelbaum,[7] Lance Miller,[11] Bruno Moraes,[12] Maria E. S. Pereira,[13]
Sergio A. Rodríguez-Torres,[14,15,16] Fabian Schmidt,[3] Huan-Yuan Shan,[17]
Matteo Viel[18,19] and Francisco Villaescusa-Navarro[18,19,20]

Affiliations are listed at the end of the paper

ABSTRACT

We present high signal-to-noise galaxy–galaxy lensing measurements of the Baryon Oscillation Spectroscopic Survey constant mass (CMASS) sample using 250 deg^2 of weak-lensing data from Canada–France–Hawaii Telescope Lensing Survey and Canada–France–Hawaii Telescope Stripe 82 Survey. We compare this signal with predictions from mock catalogues trained to match observables including the stellar mass function and the projected and two-dimensional clustering of CMASS. We show that the clustering of CMASS, together with standard models of the galaxy–halo connection, robustly predicts a lensing signal that is 20–40 per cent larger than observed. Detailed tests show that our results are robust to a variety of systematic effects. Lowering the value of $S_8 = \sigma_8\sqrt{\Omega_{\rm m}/0.3}$ compared to Planck Collaboration XIII reconciles the lensing with clustering. However, given the scale of our measurement ($r < 10\ h^{-1}$ Mpc), other effects may also be at play and need to be taken into consideration. We explore the impact of baryon physics, assembly bias, massive neutrinos and modifications to general relativity on $\Delta\Sigma$ and show that several of these effects may be non-negligible given the precision of our measurement. Disentangling cosmological effects from the details of the galaxy–halo connection, the effect of baryons, and massive neutrinos, is the next challenge facing joint lensing and clustering analyses. This is especially true in the context of large galaxy samples from Baryon Acoustic Oscillation surveys with precise measurements but complex selection functions.

Key words: gravitational lensing: weak – cosmology: observations – large-scale structure of Universe.

1 INTRODUCTION

Weak gravitational lensing is recognized as a powerful and unique cosmological tool because it is one of the few direct probes of the total mass distribution of the universe, including the dark matter component. The weak-lensing signal around galaxy ensembles, commonly referred to as galaxy–galaxy lensing (hereafter 'g-g lensing'), provides a measure of the radial distribution of total mass around galaxies. Since its first detection two decades ago by Brainerd, Blandford & Smail (1996), g-g lensing has matured from a low-signal-to-noise (S/N) novelty into a sophisticated cosmological probe with recent measurements reaching out to scales beyond 50 h^{-1} Mpc with high signal to noise (e.g. Mandelbaum et al. 2013). With new large lensing surveys such as the Dark Energy Survey (Dark Energy Survey Collaboration et al. 2016), the Kilo Degree Survey (KiDS; Kuijken et al. 2015), and the Hyper Suprime Cam (HSC) survey[1] collecting high-quality lensing data for thousands of square degrees, g-g lensing measurements will soon reach even greater precision. Space-based lensing missions such as *Euclid* (Laureijs et al. 2011) and the *Wide Field Infrared Survey Telescope* (Spergel et al. 2013) will launch within the next decade with even greater capabilities and in tandem, the Large Synoptic Survey Telescope (LSST Science Collaboration et al. 2009) will collect 20 000 deg^2 of lensing quality data.

⋆E-mail: alexie@ucsc.edu
†Hubble fellow.

[1] http://hsc.mtk.nao.ac.jp/ssp/

In parallel to these efforts, surveys such as the Baryon Oscillation Spectroscopic Survey (BOSS; Eisenstein et al. 2011; Dawson et al. 2013), have collected optical spectra for more than one million massive galaxies at $z < 1$. Within only a few years, next generation experiments such as the Dark Energy Spectroscopic Instrument (DESI; Levi et al. 2013) and the Prime Focus Spectrograph (Takada et al. 2014) will measure the redshifts of tens of millions of galaxies. Baryon Acoustic Oscillation (BAO) surveys yield exquisite measurements of galaxy clustering but also provide excellent samples for lensing studies because g-g lensing measurements are more robust when applied to lens samples with spectroscopic redshifts.

In addition, galaxy clustering and g-g lensing are large-scale structure (LSS) probes with highly complimentary capabilities: the first measures the autocorrelation of galaxies whereas the second ties galaxies to the underlying dark matter distribution. Joint analyses that take advantage of the synergies between both probes are increasingly popular for studies of the galaxy halo connection (e.g. Mandelbaum et al. 2006a; Leauthaud et al. 2012; Coupon et al. 2015; Zu & Mandelbaum 2015), to constrain cosmological parameters (e.g. Yoo et al. 2006; Cacciato et al. 2009, 2013; Mandelbaum et al. 2013; More et al. 2013), and to perform tests of general relativity (GR; e.g. Reyes et al. 2010; Blake et al. 2016).

Generally speaking, measurements of galaxy clustering and g-g lensing on non-linear scales ($r < 1\,h^{-1}$ Mpc) provide us with detailed information about the galaxy–halo connection whereas large-scale measurements ($r > 10\,h^{-1}$ Mpc) are preferred for robust cosmological constraints because they can be modelled with linear theory and are less sensitive to galaxy formation processes. However, previous work has debated about exactly where to draw the line with some studies opting to remove small-scale information entirely at the cost of larger errors (Mandelbaum et al. 2013), whereas other work has included small-scale information by marginalizing over the galaxy–halo connection (Cacciato et al. 2013; More et al. 2013, 2015). This connection is typically modelled either via halo occupation distribution (HOD; Jing 1998; Peacock & Smith 2000; Berlind & Weinberg 2002; Zheng et al. 2005; Leauthaud et al. 2011; Hearin et al. 2016) or subhalo abundance matching (SHAM; Kravtsov et al. 2004; Conroy, Wechsler & Kravtsov 2006; Behroozi, Conroy & Wechsler 2010; Reddick et al. 2013) type formalisms.

Until present, because of relatively modest lensing data sets, g-g lensing measurements have played more of an ancillary role compared to clustering measurements. However, with new rapidly expanding lensing surveys, g-g lensing is poised to play an increasingly important role in analysing $z < 1$ BAO samples. In particular, redshift space distortions (RSDs) and g-g lensing have important synergies for constraining the growth of structure. Unlike BAO measurements, RSD methods push into the semi-non-linear regime and hence are more subject to theoretical systematics associated with the complexities of galaxy bias and need to be validated against realistic galaxy mock catalogues (Alam et al. 2017). With this in mind, g-g lensing measurements on both small and large scales will be important for cosmological constraints, but also for characterizing the details of the galaxy–halo connection to help pin down theoretical systematic uncertainties for RSD. This is especially true in the context of BAO samples that have complex selection functions and that are therefore non-trivial to model using standard galaxy–halo type models.

This paper presents a high-signal-to-noise ($S/N = 30$) g-g lensing measurements for the BOSS 'constant mass' (CMASS) sample using 250 deg^2 of lensing data (Sections 2 and 3). We show that the amplitude of the lensing signal is in tension with predictions from a variety of BOSS mock catalogues that reproduce the clustering of CMASS (Section 4). This may indicate that our data prefer a low value of the amplitude of matter fluctuations at low redshifts, a failure of standard models of the galaxy–halo connection, or may be a signature of the effect of baryons on the matter distribution. A discussion of our results, including detailed tests for systematic effects, is presented in Section 5 and summarized in Section 6. We assume a flat Λ cold dark matter (ΛCDM) cosmology with $\Omega_{\mathrm{m}} = 0.31$, $\Omega_{\Lambda} = 0.69$, $H_0 = 100\,h^{-1}$ km s^{-1} Mpc^{-1}. Unless noted otherwise, distances are expressed in comoving coordinates.

2 DATA

2.1 The BOSS CMASS sample

BOSS is a spectroscopic survey of 1.5 million galaxies over 10 000 deg^2 that was conducted as part of the Sloan Digital Sky Survey-III (SDSS-III) program (Eisenstein et al. 2011) on the 2.5-m aperture Sloan Foundation Telescope at Apache Point Observatory (Gunn et al. 1998, 2006). A general overview of the BOSS survey can be found in Dawson et al. (2013) and the BOSS pipeline is described in Bolton et al. (2012). BOSS galaxies were selected from Data Release 8 (DR8, Aihara et al. 2011) *ugriz* imaging (Fukugita et al. 1996) using a series of colour–magnitude cuts (Reid et al. 2016). BOSS targeted two primary galaxy samples: the LOWZ sample at $0.15 < z < 0.43$ and the CMASS sample at $0.43 < z < 0.7$. In this paper, we focus on the high-redshift CMASS sample. As our input catalogue, we use the BOSS DR11 (Ahn et al. 2014) LSS catalogue created by the BOSS galaxy clustering working group (Anderson et al. 2014).

Because each BOSS fibre has a diameter of 62 arcsec, no two objects separated by less than this can be observed on a single plate. In addition, redshift measurements fail for a small fraction of BOSS galaxies (<2 per cent for CMASS). Because of these two effects, a small number of CMASS targets do not obtain a spectroscopic redshift.

There are various different choices for how to correct for fibre collisions and redshift failures – details can be found in Anderson et al. (2012) and Guo, Zehavi & Zheng (2012).[2] We test several methods for dealing with galaxies with missing spectroscopic redshifts and show that this correction does not have a large impact on the CMASS lensing signal (see Appendix A4). As our fiducial correction method, we adopt the same weighting scheme as the BOSS LSS working group. Namely, we upweight the galaxy nearest to each unobserved galaxy (the 'nearest neighbour' weighting method). Fibre collision and redshift-failure correction weights are denoted w_{cp} and w_{rf}, respectively.

Because our analysis is limited to relatively small scales, we do not apply the angular systematic weights (w_{sys}) or the minimum variance weights (w_{FKP}) that are used in BOSS large-scale analyses (see section 3 in Anderson et al. 2012 for details). Our weighting scheme is consistent with the one adopted for the clustering measurements of Saito et al. (2016).

2.2 Weak-lensing data

To measure the weak-lensing signal of CMASS galaxies, we use a combination of two data sets: the Canada–France–Hawaii Telescope Lensing Survey (CFHTLenS; Heymans et al. 2012; Miller et al. 2013) and the Canada–France–Hawaii Telescope Stripe 82

---

[2] Also see http://www.sdss3.org/dr9/tutorials/lss_galaxy.php.

Survey (CS82; Erben et al., in preparation). The combined area is ~250 deg^2 and both data sets use i'-band imaging from the CFHT MegaCam instrument (Boulade et al. 2003) taken under excellent seeing conditions (seeing 0.6–0.7 arcsec). Data reduction and shape measurements for both surveys were performed homogeneously using the state-of-the-art weak-lensing pipeline developed by the CFHTLenS collaboration which employs the *lens*fit Bayesian shape measurement algorithm (Heymans et al. 2012; Miller et al. 2013). Differences between CFHTLenS and CS82 that are of relevance for this work are the i'-band depth, the source of additional photometry for photo-z measurements, and the degree of overlap with the BOSS survey. Further details are now described below.

2.2.1 CFHTLenS weak-lensing catalogue

The CFHTLenS weak-lensing catalogues are based on deep multi-colour data obtained as part of the CFHT Legacy Survey (CFHTLS). This survey spans 154 deg^2 in five optical bands ($u^*g'r'i'z'$) with a 5σ point source limiting magnitude of $i' \sim 25.5$. Each Mega-Cam pointing is roughly 1 deg^2 in area and has a pixel size of 0.187 arcsec. The CFHTLS Wide survey consists of four separate patches on the sky known as W1, W2, W3 and W4 (63.8, 22.6, 44.2 and 23.3 deg^2, respectively). BOSS fully overlaps with the W4 field, partially overlaps with W1 and W3, and only has a small amount of overlap with W2. In this paper, we use the overlap regions in W1, W3 and W4. Details on the image reduction, weak-lensing shape measurements and photometric redshifts can be found in Erben et al. (2013), Heymans et al. (2012), Miller et al. (2013) and Hildebrandt et al. (2012).

We download the publicly available CFHTLenS weak-lensing shear catalogues.[3] Following Heymans et al. (2012), we apply an additive calibration correction factor, c_2, to the ϵ_2 shape component on a galaxy-by-galaxy basis.[4] For each galaxy, we also compute a multiplicative shear calibration factor as a function of the signal-to-noise ratio and size of the source galaxy, $m(\nu_{SN}, r)$.[5] The calibration correction factor for ϵ_2 and the multiplicative shear calibration factor, m, are computed separately for CFHTLenS and CS82. The values for the m correction factor are given in Section 3.3 and represent a 3–7.5 per cent increase in $\Delta\Sigma$. Following Velander et al. (2014), we do not reject pointings that did not pass the requirements for cosmic shear. The CFHTLenS *lens*fit catalogues contain a lensing (inverse variance) weight w which includes both the intrinsic shape dispersion as well as the ellipticity measurement error.

2.2.2 CS82 weak-lensing catalogue

The SDSS contains a subregion of 275 deg^2 on the Celestial Equator in the southern galactic cap known as 'Stripe 82' (Abazajian et al. 2009). This region was repeatedly imaged during the Fall months when the north galactic cap was not observable. The co-addition of these data reaches $r \sim 23.5$, about 2 mag fainter than the SDSS single pass data (Annis et al. 2014) but has an r-band median seeing of 1.1 arcsec.

The CS82 survey was designed with the goal of complementing existing Stripe 82 SDSS *ugriz* imaging with high-quality i'-band imaging suitable for weak-lensing measurements. CS82 is built from 173 MegaCam i'-band images and corresponds to an area of 160 deg^2 (129.2 deg^2 after masking out bright stars and other image artefacts). The point spread function for CS82 varies between 0.4 and 0.8 arcsec over the entire survey with a median seeing of 0.6 arcsec. The limiting magnitude of the survey is $i \sim 24.1$.[6]

Image processing is largely based on the procedures presented in Erben et al. (2009) and shear catalogues were constructed using the same weak-lensing pipeline developed by the CFHTLenS collaboration using the *lens*fit Bayesian shape measurement method (Miller et al. 2013). We compute m and c_2 for each galaxy and construct a source catalogue for CS82 in the same fashion as for CFHTLenS. The CS82 source galaxy density is 15.8 galaxies arcmin^{-2} and the effective weighted galaxy number density (see equation 1 in Heymans et al. 2012) is 12.3 galaxies arcmin^{-2}. Note that these numbers do not yet include any photo-z quality cuts. These are described in the following section.

2.2.3 Photometric redshifts

Photometric redshifts for the CFHTLenS source catalogue have been calculated by Hildebrandt et al. (2012) using the Bayesian photometric redshift software BPZ (Benítez 2000; Coe et al. 2006). Photo-zs for CS82 have been calculated by Bundy et al. (2015), also using BPZ. For a redshift estimate, we use Z_B, the peak of the posterior distribution given by BPZ. In addition to Z_B, we will use the 95 per cent confidence limit (noted σ_{95}) on Z_B as well as the BPZ ODDS parameter (a measure of the peakiness of the probability density function provided by BPZ). The ODDS parameter varies between 0 and 1 and galaxy samples with larger ODDS values have reduced catastrophic outlier fractions (e.g. Margoniner & Wittman 2008).

Determining the level of systematic error due to photometric redshifts is often one of the most uncertain aspects of a galaxy–galaxy weak-lensing analysis (e.g. Nakajima et al. 2012). Fortunately, the CS82 survey overlaps with a number of existing spectroscopic surveys which can be used to assess the quality of our photometric redshifts. We compile a set of high-quality spectroscopic redshifts that overlap with CS82 from the BOSS DR12 data release (Alam et al. 2015), VVDS (Le Fèvre et al. 2004), DEEP2 (Newman et al. 2013) and PRIMUS (Coil et al. 2011). For VVDS, DEEP2 and PRIMUS, we select galaxies with a redshift quality flag greater than or equal to 3. Our combined spectroscopic sample contains a total of 11 694 objects.[7] Among these data sets, the DEEP2 redshifts are the most useful for our purpose. The DEEP2 spectroscopic redshift catalogue contains galaxies to $R_{AB} = 24.1$ which spans the full magnitude range of our source sample. However, the DEEP2 sample is also colour selected to target galaxies at $z > 0.7$. Because we study lens galaxies between $z = 0.43$ and $z = 0.7$, a large majority of our source galaxies have redshifts with $z > 0.7$ which is well matched to the DEEP2 selection. Fig. 1 displays a comparison between z_{spec} and z_{phot} for our fiducial CS82 source catalogue (which includes a cut of ODDS > 0.5).

---

[3] http://www.cadc-ccda.hia-iha.nrc-cnrc.gc.ca/community/CFHTLens/query.html

[4] Equation (19) in Heymans et al. (2012) assumes a galaxy size r in arcseconds and the r_0 parameter has units of arcseconds.

[5] When using the parameters to compute m provided in Miller et al. (2013), r corresponds to the scale-length field in the CFHTLenS catalogues in pixel units.

[6] The limiting magnitude is defined as the 5σ detection limit in a 2 arcsec aperture via $m_{lim} = ZP - 2.5\log(5)\sqrt{N_{pix}\sigma_{sky}}$, where N_{pix} is the number of pixels in a circle of radius 2 arcsec, σ_{sky} is the sky background noise variation, and ZP is the zero-point.

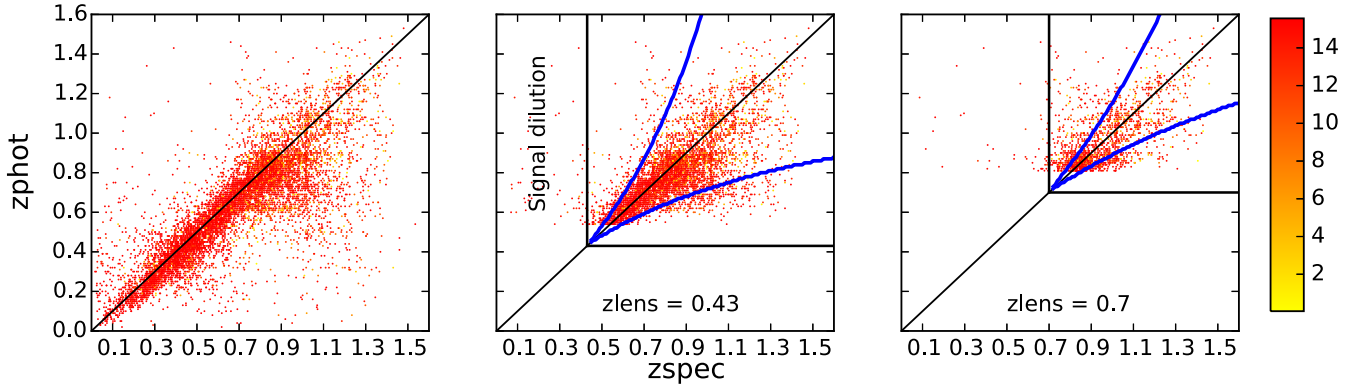[7] 207 galaxies from BOSS, 5328 from DEEP2, 4942 from PRIMUS and 1217 from VVDS.

Figure 1. Comparison between $z_{\rm spec}$ and $z_{\rm phot}$ for the CS82 source catalogue. Galaxies are colour coded according to their lensing weight w (with values indicated by the colour bar on the right-hand side). Our CMASS lens sample is located at redshifts $0.43 < z_{\rm L} < 0.7$. The middle and right-hand panels display a comparison between $z_{\rm spec}$ and $z_{\rm phot}$ for 'background' source galaxies for lens redshifts of $z_{\rm L} = 0.43$ and $z_{\rm L} = 0.7$. To select background galaxies, we require that $z_{\rm S} > z_{\rm L} + 0.1$ and $z_{\rm S} > z_{\rm L} + \sigma_{95}/2.0$. Source galaxies that satisfy this cut but which have a true redshift $z_{\rm spec} < z_{\rm L}$ will dilute the lensing signal. These correspond to objects located to the left of the vertical solid lines (middle and right-hand panels) and represent less than 3 per cent of our source sample for lenses at $z_{\rm L} = 0.7$. Our fiducial cut-off ODDS>0.5 reduces the number of galaxies located in this region. Solid blue curves represent the locus corresponding to a 30 per cent bias on $\Delta\Sigma$. While we do have some source galaxies located outside the cone formed by the blue curves, what is important for $\Delta\Sigma$ is that mean value of $\Sigma_{\rm crit}$ (averaged over the full source population) is un-biased (see Appendix A2 and equation A3).

When computing $\Delta\Sigma$, we do not integrate over the full redshift probability distribution function, $p(z)$, of source galaxies. Indeed, photo-z codes do not automatically provide accurate estimates for $p(z)$. For this reason, integrating over $p(z)$ does not automatically guarantee a more accurate result. Instead, we use a point estimate as our source redshift, but we use an appropriately re-weighted version of the spectroscopic data set described above, to test for biases in our computation of $\Delta\Sigma$. The details of this computation are given in Appendix A2. Using our combined set of spectroscopic redshifts, we estimate that photo-z errors cause our $\Delta\Sigma$ values to be overestimated by $\sim$3 per cent. This estimate includes the dilution of the signal by source galaxies that have $z_{\rm spec} < z_{\rm L}$ but $z_{\rm phot} > z_{\rm L}$ where $z_{\rm L}$ is the lens redshift.

Finally, we also perform a series of tests to demonstrate that our lensing signal is robust to a variety of different cuts on the photo-z catalogue. The results of these tests are presented in Appendix A2. No statistically significant systematic trends are found for any of the tests that we have implemented.

2.2.4 Source catalogue and background selection

We construct a source catalogue by applying the following cuts: MASK$\leq$1, FITCLASS=0, $i' < 24.7$, and $w > 0$. Here, FITCLASS is a flag to remove stars but also to select galaxies with well-measured shapes (see details in Miller et al. 2013) and MASK is a masking flag. In addition, we also require that each source galaxy has a photo-z estimate and we apply a fiducial photo-z quality cut of ODDS >0.5. Our lensing signals are robust to the choice of this ODDS parameter cut (see Appendix A2). After applying these cuts, the CFHTLenS and CS82 source catalogues correspond, respectively, to effective weighted galaxy number densities[8] of $n_{\rm eff} = 10.8$ galaxies arcmin^{-2} and $n_{\rm eff} = 4.5$ galaxies arcmin^{-2}.

To minimize any dilution of our lensing signal due to photo-z uncertainties, we perform background selection by requiring that $z_{\rm S} > z_{\rm L} + 0.1$ and $z_{\rm S} > z_{\rm L} + \sigma_{95}/2.0$ where $z_{\rm L}$ is the lens redshift,

$z_{\rm S}$ is the source redshift, and σ_{95} is the 95 per cent confidence limit on the source redshift. This fiducial scheme for separating background sources from lens galaxies will be referred to as ZCUT2. In Appendix A2, we show that our lensing signals are robust to the exact details of this cut, which suggests that our lensing signal is not strongly affected by contamination from source galaxies with $z_{\rm spec} < z_{\rm L}$ but $z_{\rm phot} > z_{\rm L}$. Our tests with spectroscopic redshifts in Appendix A2 confirms and quantifies this statement.

We do not apply a correction factor to account for a dilution effect from source galaxies that are actually physically associated with our lens sample (the so-called 'boost correction factor'). A detailed justification of this choice is presented in Appendix A1.

3 COMPUTATION OF $\Delta\Sigma$

3.1 Stacking procedure

Our stacking procedure closely follows the methodology outlined in Leauthaud et al. (2012) and we refer to that work for in-depth details. The primary difference with respect to Leauthaud et al. (2012) is that here we stack the g–g lensing signal in comoving instead of physical coordinates. The g–g lensing signal that we measure yields an estimate of the mean *surface mass density contrast* profile:

$$\Delta\Sigma(r) \equiv \overline{\Sigma}(< r) - \overline{\Sigma}(r). \tag{1}$$

Here, $\overline{\Sigma}(r)$ is the azimuthally averaged and projected surface mass density at radius r and $\overline{\Sigma}(< r)$ is the mean projected surface mass density within radius r (Miralda-Escude 1991; Wilson et al. 2001). The relationship between the tangential shear, $\gamma_{\rm t}$, and $\Delta\Sigma$ is given by

$$\Delta\Sigma = \gamma_{\rm t}\Sigma_{\rm crit}, \tag{2}$$

where $\Sigma_{\rm crit}$ is the *critical surface mass density* which in comoving coordinates is expressed by

$$\Sigma_{\rm crit} = \frac{c^2}{4\pi G} \frac{D_A(z_{\rm S})}{D_A(z_{\rm L}) D_A(z_{\rm L}, z_{\rm S})(1 + z_{\rm L})^2}, \tag{3}$$

where $D_A(z_{\rm L})$ and $D_A(z_{\rm S})$ are angular diameter distances to the lens and source and $D_A(z_{\rm L}, z_{\rm S})$ is the angular diameter distance between the lens and source.

---

[8] Here, we use $n_{\rm eff}$ as defined by equation (1) in Heymans et al. (2012). An alternative definition of $n_{\rm eff}$ is given by equation (9) in Chang et al. (2013).
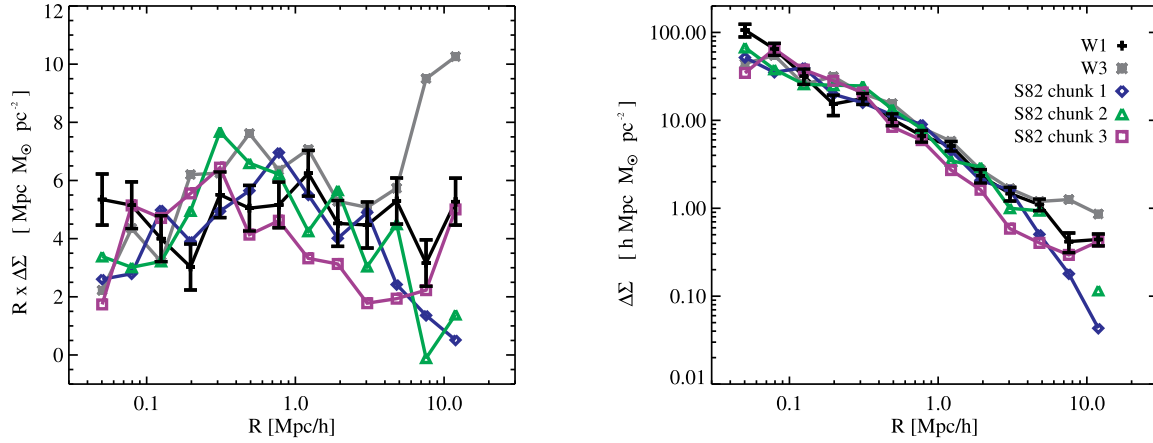
Figure 2. CMASS g-g lensing signal calculated in five independent subregions of roughly equal area (two regions from CFHTLenS and three from CS82). Each patch is of the order of ~40–50 deg². Because there are not enough bootstrap regions per subregion to compute bootstrap errors, we simply show the typical shape noise errors for one of the patches (black data points) which underestimates the errors on large scales. As can be seen, there is a significant amount of field-to-field variance between the five independent patches. However, importantly, there is no obvious systematic trend *between* CFHTLenS and CS82 patches.

The *lens*fit algorithm provides an inverse variance weight, w, which can be used to optimally weight shear measurements. For a given lens i and a given source j, the inverse variance weight for $\Delta\Sigma$ can be derived from equation (2) and is equal to $w_{\mathrm{ds},ij} = w_j \Sigma_{\mathrm{crit},ij}^{-2}$. We use w_{ds} to compute $\Delta\Sigma$ via a weighted sum over all lens–source pairs:

$$\Delta\Sigma = \frac{\sum_{i=1}^{N_{\mathrm{L}}} \sum_{j=1}^{N_{\mathrm{S}}} w_{\mathrm{ds},ij} \times \gamma_{\mathrm{t},ij} \times \Sigma_{\mathrm{crit},ij}}{\sum_{i=1}^{N_{\mathrm{L}}} \sum_{j=1}^{N_{\mathrm{S}}} w_{\mathrm{ds},ij}}, \qquad (4)$$

where N_{L} is the number of lens galaxies and N_{S} is the number of source galaxies. Each lens contributes a different effective weight in this sum. This topic is discussed further in Appendix A5.

We compute $\Delta\Sigma$ in 13 logarithmically spaced radial bins from $R_1 = 0.04 \ h^{-1}$ Mpc to $R_2 = 15 \ h^{-1}$ Mpc. The limit on our outer radial bin is set by the size of our bootstrap regions and is discussed in the following section.

3.2 Bootstrap errors and variance in the lensing signal

The covariance matrix and correlation matrix for our data vector of $\Delta\Sigma$ values will be noted as **C** and $\mathbf{C}_{\mathrm{corr}}$, respectively. We estimate **C** from the data using stratified bootstrap. Our bootstrap errors should account for the effects of correlated shape noise as well as for field-to-field variance in the lensing signal.

We divide CFHTLenS and CS82 into 74 roughly equal area bootstrap regions (45 for CS82 and 29 for CFHTLenS). Each region is ~3–4 deg² which corresponds to regions with transverse comoving dimensions of the order of 40–60 h^{-1} Mpc at the redshift of the CMASS sample. Our bootstrap regions are designed as a compromise between two competing requirements. First, in order to ensure that the bootstrap samples are independent, we require the size of the bootstrap regions to be larger than the maximum scale used in the measurement (15 h^{-1} Mpc). Secondly, we need a large number of bootstrap regions in order to reduce the noise in our evaluation of the covariance matrix. However, this second requirement goes in the direction of requiring many regions, which will thus necessarily have to be smaller. Satisfying these two requirements determines the maximum scale to which we compute our g-g lensing signal. Unless specified otherwise, errors on our g-g lensing signals are derived using 10 000 resamplings of these bootstrap regions.

Although CFHTLenS and CS82 are fairly large surveys,[9] we find that there is still a large field-to-field variance in the amplitude of the CMASS lensing signal.[10] To highlight this fact, we compute the CMASS g-g lensing signal separately for W1 and W3 as well as for three independent Stripe 82 patches that roughly match the areas of W1 and W3. Each of these patches contains about 4000 CMASS galaxies. Fig. 2 presents the CMASS g-g lensing signal for each of these five subregions. As can be seen from Fig. 2, there is a significant amount of variance between the g-g lensing signals of each of these five independent patches. However, importantly, there is no obvious systematic trend *between* CFHTLenS and CS82 patches. This test suggests that differences between the lensing signals from CFHTLenS and CS82 can be attributed to field-to-field variance and not systematic effects between the two surveys.

Our bootstrap errors should account for sample variance effects. However, because our analysis is based on a subregion of the full BOSS footprint, possible large-scale variations in the properties of the CMASS sample may be a concern. Fig. 3 shows that the number density of CMASS within the CS82 footprint closely follows the number density of the full CMASS sample. We conclude from Fig. 3 that substantial differences between the CS82 CMASS sample and the full DR12 CMASS sample are an unlikely possibility.

3.3 Combined signal from CS82 and CFHTLenS

We first compute the CMASS g-g lensing signal separately for CFHTLenS and CS82. The multiplicative shear calibration factor is applied separately for each survey.[11] Because the CS82 source catalogue is limited by photo-zs and not shape measurements, CS82 source galaxies have a higher mean signal to noise than CFHTLenS source galaxies. As a result, CS82 has a smaller overall calibration factor compared to CFHTLenS. For CFHTLenS,
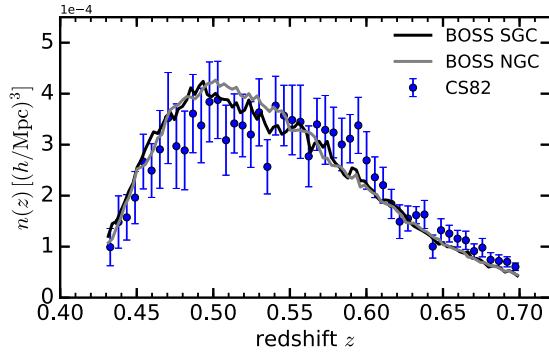

Figure 3. Number density of CMASS galaxies within the CS82 footprint compared to the number density for the full DR12 sample. Black and grey solid lines show the dn/dz for the north and south galactic cap, respectively. Errors reflect the variance of dn/dz between 24 independent BOSS patches that each have the same area as CS82.
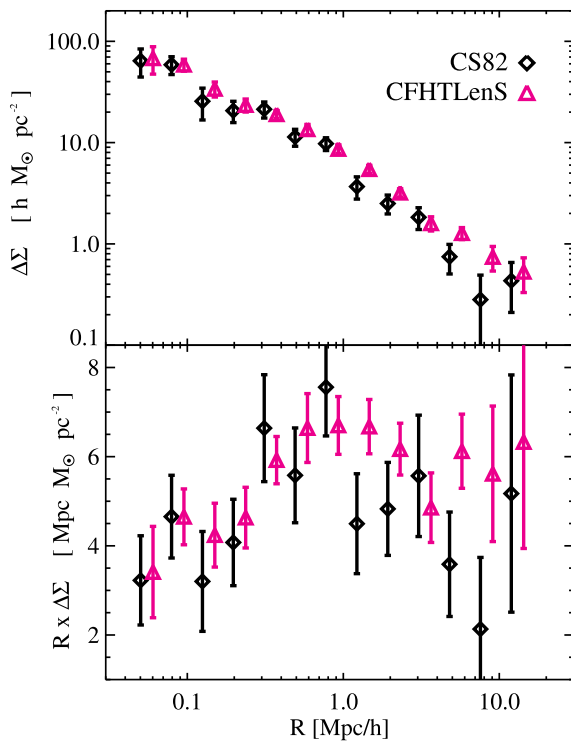

Figure 4. Comparison between the CMASS g-g lensing signal from CS82 (black diamonds) and from CFHTLenS (magenta triangles). The CFHTLenS data point are slightly offset for visual clarity. The signals agree well on small scales but there is moderate amplitude difference at larger scales which we attribute to field-to-field variance.

$1 + m_{cfhtls} \sim 0.93$ which results in a 7.5 per cent increase in $\Delta\Sigma$. For CS82, $1 + m_{cs82} \sim 0.97$ which results in a 3 per cent increase in $\Delta\Sigma$.

Fig. 4 displays the CMASS g-g lensing signal from CFHTLenS and CS82. The signals agree well on small scales but there is moderate amplitude difference at large scales which we attribute to field-to-field variance as discussed in the previous section. Because we do not have enough bootstrap regions to compute resampling errors for CFHTLenS and CS82 separately, the errors displayed in Fig. 4 correspond to shape noise errors which will underestimate the true variance on large scales. Also, from the combined analysis, we expect the five outer points in these g-g lensing signals to

be moderately correlated (see Fig. 6). Given this caveat, it is difficult to ascertain the exact significance of the large-scale amplitude difference between the two surveys. Instead, what we take away from Fig. 4 is that there is no evidence for a global amplitude shift between the lensing signals from CFHTLenS and CS82.

Having convinced ourselves from Fig. 2 that there are no obvious systematic trends between the two surveys, we now proceed to combine the g-g lensing signal from CS82 and CFHTLenS. There are 13 775 CMASS galaxies from CS82 and 10 507 from CFHTLenS that are included in the weak-lensing stack. Importantly, by combining the two surveys, we gain a wider area with which to compute bootstrap errors on the combined signal (74 bootstrap regions for the combined sample).

Fig. 5 displays the combined g-g lensing signal. The combination of CFHTLenS and CS82 yields a high S/N measurement of the lensing signal for CMASS. The S/N of the signal is

$$\frac{S}{N} = \left(x^T \mathbf{C}^{-1} x\right)^{1/2}, \qquad (5)$$

where x is the vector of $\Delta\Sigma$ values in each radial bin and $\mathbf{C}$ is the covariance matrix. There are 13 data points in our stack and the relative error on each data point is 10–20 per cent. Our overall lensing signal is detected with a signal to noise of $S/N = 30$. For comparison purposes, the S/N of the g-g lensing signals used in the cosmological analysis of Mandelbaum et al. (2013) had $S/N \sim 25$.[12]

We do not have enough bootstrap regions to constrain the full covariance matrix, but we can constrain the dominant off-diagonal terms. At small scales, we expect the data points to be uncorrelated (e.g. Viola et al. 2015). On large scales, however, we expect non-zero off-diagonal terms due to sample variance and correlated shape noise which arises when source galaxies appear in multiple radial bins (Jeong, Komatsu & Jain 2009; Mandelbaum et al. 2013). We compute the correlation matrix, $\mathbf{C}_{corr}$, for our signal and then apply a boxcar smoothing algorithm with a length of one bin in radius to this matrix, to reduce the noise (see Mandelbaum et al. 2013 for a similar procedure). We then truncate the correlation matrix to values greater than 0.2 since we do not expect to constrain these terms.[13] Because we reduce the noise in the correlation matrix directly, we do not attempt to apply any noise bias corrections when inverting $\mathbf{C}$ (for example see Hartlap, Simon & Schneider 2007). The result is displayed in Fig. 6. As expected, the outer data points are moderately correlated. The dominant terms in the correlation matrix for the overall signal are given in Table 1.

We also compute the CMASS lensing signal in three redshift bins: zbin1= [0.43, 0.51], zbin2=[0.51, 0.57], and zbin3=[0.57, 0.7]. We have checked that the multiplicative shear calibration factor, m, does not vary strongly over this redshift baseline for either CFHTLenS or CS82 and that the same calibration factor that we used for the single wide redshift bin can be used for these more narrow redshift bins. The g-g lensing signal for each of these redshifts bins is presented in the right-hand side of Fig. 5 and the data points for our g-g lensing measurements are provided in Table 1. Interestingly, the amplitude of the g-g lensing signal does not vary strongly with redshift – we will return to this point in Section 5.3.

---

[12] Over the radial range 0.1–70 Mpc h^{-1}, including small-scale information that was not used in the cosmological analysis, the S/N of the Mandelbaum et al. (2013) measurement is $S/N = 36$.

[13] Our results are unchanged whether or not we apply the smoothing and truncation to $\mathbf{C}_{corr}$.
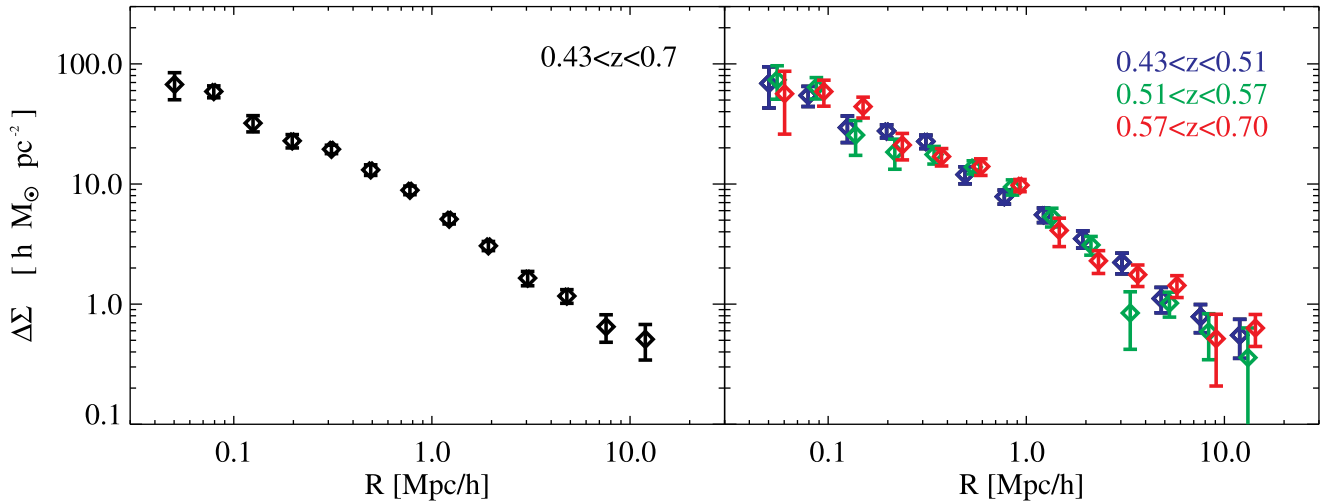
Figure 5. Stacked weak-lensing signal for CMASS using both CS82 and CFHTLenS. Left: lensing signal for CMASS in the redshift range $0.43 < z < 0.7$. Right: combined lensing signal for CMASS in three redshift bins. Data points in each redshift bin have been slightly offset for visual clarity. Errors are computed via bootstrap.
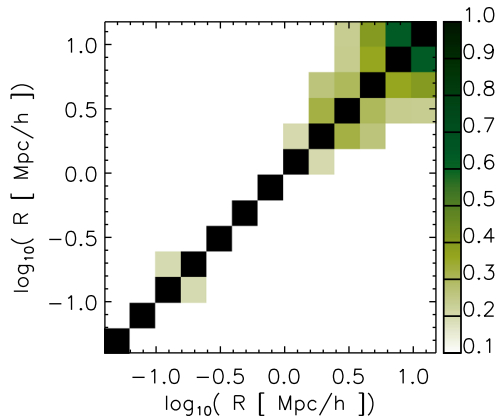

Figure 6. Correlation matrix, $\mathbf{C}_{corr}$, computed via bootstrap, smoothed over one pixel scale, and truncated to values greater than 0.2. The outer five data points in our g-g lensing are moderately correlated due to sample variance and correlated shape noise. The inner data points are uncorrelated and the errors on small scales are dominated by shape noise.

4 RESULTS: COMPARISON WITH PREDICTIONS FROM MODELS TRAINED ON GALAXY CLUSTERING

We now compare our lensing signal with predictions from mock catalogues tailored to match the clustering of CMASS (Reid et al. 2014; Rodríguez-Torres et al. 2016; Saito et al. 2016; Alam et al. 2017). These mock catalogues were created by independent teams, using a range of methodologies, cosmologies, *N*-body simulations (with varying resolutions), and were all designed to reproduce the clustering of CMASS on the scales relevant for this work ($r < 30\,h^{-1}$ Mpc). Two mocks employ SHAM whereas others employ an HOD-based method. The cosmology of these mocks ranges between a WMAP 5 cosmology (Komatsu et al. 2009) with $\Omega_m = 0.27$ and a Planck-like cosmology (Planck Collaboration XIII 2016) with $\Omega_m = 0.31$. Table 2 summarizes the parameters of the various *N*-body simulations used to generate our predictions. We do not use the quick particle mesh (White, Tinker & McBride 2014) or PATCHY (Kitaura, Yepes & Prada 2014) mocks from the BOSS collaboration because these do not have the necessary resolution to reproduce

the galaxy–matter correlation function on the scales of interest. We begin with an overview of the mocks used for our comparison.

4.1 Overview of CMASS mock catalogues

Reid et al. (2014) performed a joint analysis of the projected and the anisotropic clustering (monopole and quadrupole) of CMASS on scales from 0.8 to 32 h^{-1} Mpc. Their analysis was performed by populating an *N*-body simulation at $z = 0.55$ with mock galaxies based on a standard HOD-type prescription. A single redshift-independent HOD model was assumed with a number density of $\bar{n} \sim 4 \times 10^{-4}(h^{-1}\,\mathrm{Mpc})^{-3}$. Their mock catalogues were randomly down-sampled along one of the axis of the simulation to match the CMASS dn/dz. This procedure assumes that CMASS galaxies at all redshifts are a random subsample drawn from a single population. Reid et al. (2014) performed fits using two different simulations: a 'MedRes' *N*-body simulation ($\Omega_m = 0.292$, $\sigma_8 = 0.82$) and a 'HiRes' simulation with a Planck cosmology ($\Omega_m = 0.308\,51$, $\sigma_8 = 0.8288$, Planck Collaboration XVI 2014). We compare with the predictions from the best-fitting models for both simulations. Reid et al. (2014) also perform several tests to verify the robustness of their results to extensions of the standard HOD model. In one such test, they consider a scenario in which 20 per cent of centrals in massive haloes are not CMASS-selected galaxies (labelled 'cen/sat' test in their paper). In this test, a central galaxy is not required for a given halo to host a satellite galaxy. We compare with both the fiducial model from Reid et al. (2014) as well as with the cen/sat model but find that both models generate similar predictions for the lensing signal.

Saito et al. (2016) present a joint modelling of both the projection correlation function of CMASS (w_p^{CMASS}) and of the galaxy stellar mass function (SMF) using SHAM. To perform SHAM, Saito et al. (2016) use the galaxy SMF[14] computed by Leauthaud et al. (2016) from the Stripe 82 Massive Galaxy Catalog[15] (s82-MGC, Bundy

---

[14] Using SHAM in the mass range relevant for CMASS requires a measurement of the total (all galaxies, not just CMASS) galaxy SMF down to stellar masses of roughly $\log_{10}(M_*/\mathrm{M}_\odot) \sim 10.8$.
[15] Publicly available at www.massivegalaxies.com.

Table 1. Combined CS82+CFHTLenS g-g lensing measurements for CMASS. Errors are estimated via bootstrap (Section 3.2). The dominant terms in the correlation matrix for the overall signal are: $\mathbf{C}_{\mathrm{corr}}[12, 13] = 0.64$, $\mathbf{C}_{\mathrm{corr}}[11, 13] = 0.42$, $\mathbf{C}_{\mathrm{corr}}[10, 13] = 0.25$, $\mathbf{C}_{\mathrm{corr}}[11, 12] = 0.38$, $\mathbf{C}_{\mathrm{corr}}[10, 12] = 0.25$, $\mathbf{C}_{\mathrm{corr}}[10, 11] = 0.30$, $\mathbf{C}_{\mathrm{corr}}[9, 11] = 0.26$, $\mathbf{C}_{\mathrm{corr}}[9, 10] = 0.32$. These values can be combined with the errors given below to form the covariance matrix for the signal measured over the full redshift range $0.43 < z < 0.7$. Note that these errors do not include a systematic uncertainty from photo-zs. In Appendix A2, we estimate this systematic uncertainty to be of the order of 3 per cent. Our conservative estimate for the total fractional systematic error on $\Delta\Sigma$ is 5–10 per cent.

Bin number	R (h^{-1} Mpc)	$\Delta\Sigma$ ($h\,\mathrm{M}_\odot\,\mathrm{pc}^{-2}$) $0.43 < z < 0.7$	$\Delta\Sigma$ ($h\,\mathrm{M}_\odot\,\mathrm{pc}^{-2}$) $0.43 < z < 0.51$	$\Delta\Sigma$ ($h\,\mathrm{M}_\odot\,\mathrm{pc}^{-2}$) $0.51 < z < 0.57$	$\Delta\Sigma$ ($h\,\mathrm{M}_\odot\,\mathrm{pc}^{-2}$) $0.57 < z < 0.7$
1	0.05	67.16 ± 16.77	67.95 ± 25.50	73.43 ± 23.01	57.03 ± 29.74
2	0.08	58.98 ± 6.73	54.83 ± 10.58	63.67 ± 13.04	59.08 ± 14.40
3	0.13	32.12 ± 4.95	29.61 ± 7.33	25.31 ± 8.22	44.26 ± 8.71
4	0.20	22.95 ± 2.90	27.69 ± 3.45	18.57 ± 5.14	21.14 ± 5.25
5	0.31	19.50 ± 1.58	22.71 ± 2.92	17.59 ± 2.98	16.92 ± 2.80
6	0.49	13.13 ± 1.33	12.02 ± 1.95	13.84 ± 1.73	13.98 ± 2.22
7	0.77	8.88 ± 0.74	7.87 ± 1.06	9.46 ± 1.36	9.75 ± 1.14
8	1.22	5.11 ± 0.45	5.56 ± 0.76	5.34 ± 0.96	4.12 ± 1.09
9	1.93	3.06 ± 0.27	3.50 ± 0.58	3.11 ± 0.55	2.31 ± 0.49
10	3.04	1.65 ± 0.22	2.23 ± 0.43	0.85 ± 0.42	1.76 ± 0.35
11	4.80	1.17 ± 0.15	1.12 ± 0.26	1.03 ± 0.24	1.43 ± 0.30
12	7.57	0.65 ± 0.17	0.79 ± 0.21	0.60 ± 0.25	0.52 ± 0.31
13	11.94	0.51 ± 0.17	0.55 ± 0.20	0.37 ± 0.28	0.64 ± 0.19

Table 2. Simulation parameters for BOSS mock catalogues used in Fig. 7.

Parameter	R14 MedRes	R14 HiRes	S16 MDR1	S16 updated MDPL2	RT16 BigMDPL	A16 MedRes
L_{box} (h^{-1} Mpc)	1380	677.7	1000	1000	2500	1380
N_{p}	2048^3	2048^3	2048^3	3840^3	3840^3	2048^3
Ω_{m}	0.292	0.308 51	0.27	0.31	0.307	0.292
σ_8	0.82	0.8288	0.82	0.82	0.829	0.82
z_{box}	0.550	0.547	0.534	0.457, 0.523, 0.592	0.505, 0.547, 0.623	0.550

et al. 2015). They account for the stellar mass incompleteness of CMASS by down-sampling mock galaxies according to their assigned stellar mass to match the redshift-dependent CMASS SMFs. The Saito et al. (2016) analysis used a single snapshot ($z = 0.534$) from the publicly available 'MDR1' MultiDark simulation (Prada et al. 2012; Riebe et al. 2013) with a flat WMAP 5 ΛCDM cosmology (Komatsu et al. 2009). The Saito et al. (2016) mock catalogues simultaneously reproduce $w_{\mathrm{p}}^{\mathrm{CMASS}}$, the galaxy SMF, as well as the redshift-dependent CMASS SMFs (and hence also reproduce the overall CMASS number density as a function of redshift).

In addition, we also compare with an updated version of Saito et al. (2016) which uses the MDPL2 simulation from the MultiDark suite. MDPL2 has the same box size ($L_{\mathrm{box}} = 1\,h^{-1}$ Gpc) as MDR1 but has an improved resolution compared to MDR1 ($N_{\mathrm{par}} = 3840^3$). The ΛCDM cosmology in MDPL2 is consistent with Planck Collaboration XIII (2016). MDPL2 keeps snapshots more frequently than MDR1 and has more snapshots covering the CMASS redshift range. As opposed to the MDR1 mock, here we use three different snapshots ($z = 0.457$, $z = 0.523$, $z = 0.592$) and compute an updated version of the Saito et al. (2016) mock catalogues by abundance matching each of these snapshots.

Rodríguez-Torres et al. (2016) also use SHAM to build a CMASS mock catalogue that is designed to reproduce the monopole of the redshift-space correlation function. Their mock is created from a light-cone built from 20 outputs of the BigMDPL simulation (Klypin et al. 2016) and accounts for the geometry of the BOSS survey as well as for veto masks. To perform SHAM, Rodríguez-Torres et al. (2016) compute the galaxy SMF using stellar masses

from the Portsmouth DR12 catalogue (Maraston et al. 2013). In a similar fashion to Saito et al. (2016), the stellar mass completeness of CMASS is modelled by down-sampling mock galaxies to reproduce the observed number densities as a function of stellar mass. To compute the lensing predictions from this mock, we use snapshots at three different redshifts $z = 0.5053$, $z = 0.5470$ and $z = 0.6226$.

Alam et al. (2017) build a CMASS mock catalogue using a standard four parameter HOD prescription. Their mock is based on the same 'MedRes' simulation employed by Reid et al. (2014) but they use a different procedure for populating this simulation with mock galaxies. Although Reid et al. (2014) place satellite galaxies on randomly selected dark matter particles, Alam et al. (2017) place satellite galaxies following a Navarro–Frenk–White profile (NFW; Navarro, Frenk & White 1997). Whereas Reid et al. (2014) uses haloes identified via a spherical-overdensity method, Alam et al. (2017) use haloes identified using a friends-of-friends method with halo masses adjusted following More et al. (2011). The HOD parameters used by Alam et al. (2017) are tuned to match the projected correlation function, w_p^{CMASS}.

Among the various studies considered here, Saito et al. (2016) and Rodríguez-Torres et al. (2016) are the only two that explicitly model the stellar mass incompleteness of CMASS as a function of redshift. The main differences between the two approaches are: the size of the N-body simulation (representing a trade-off between volume and resolution), the methodology for including scatter between galaxy mass and halo mass in SHAM, and the origin of CMASS stellar masses. In particular, the choice of a stellar mass estimator can lead to important differences in the galaxy SMF (see fig. 15 in
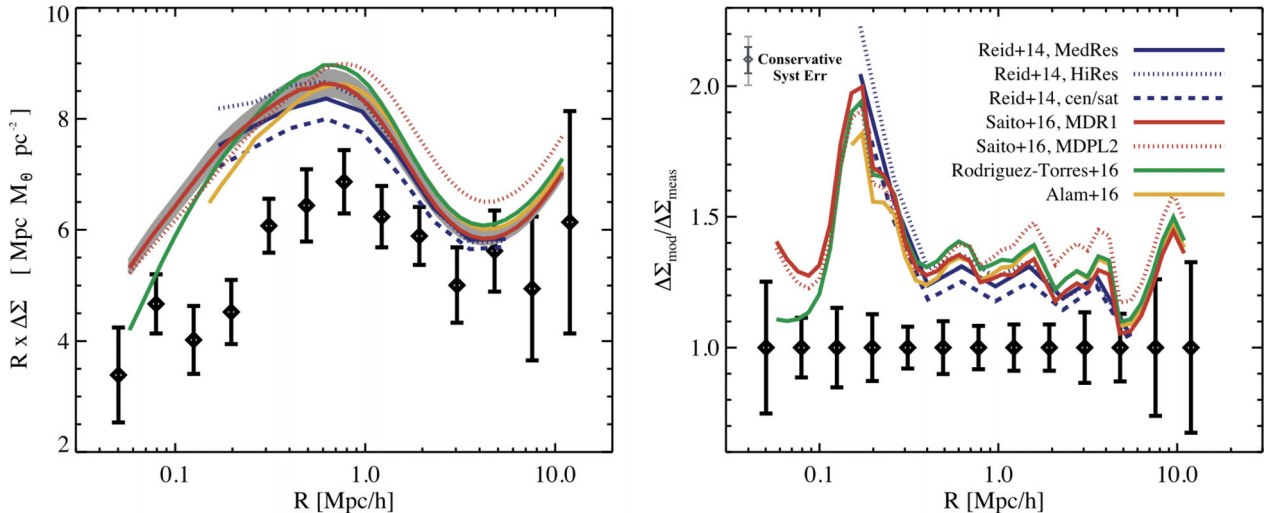
Figure 7. Comparison of the g-g lensing signal with predictions from galaxy–halo models constrained by the clustering of CMASS. The grey shaded region represents models drawn from the 68 per cent confidence region for the Saito et al. (2016) MDR1 model. The 'spike' in the predictions in the right-hand panel is simply cause by a downward fluctuation of the measured lensing signal at $r \sim 0.2\ h^{-1}$ Mpc as can be seen in the left-hand panel. Regardless of the methodology (SHAM or HOD), the adopted cosmology, or the resolution of the *N*-body simulation, models constrained by the clustering of CMASS predict a lensing amplitude that is larger by $\sim$20–40 per cent than our measurement. This is not caused by different assumptions regarding *h*. The measurement and model predictions both assume a comoving length-scale for *R* and for $\Delta\Sigma$. Our code for computing $\Delta\Sigma$ yields the same result as an independent derivation by one of our co-authors. In Section A6, we show that CS82 lensing gives consistent results compared to SDSS. Finally, our code for computing model predictions yields the same result as the HALOTOOLS software package (Hearin et al. 2016).

Leauthaud et al. 2016 for example). Both studies adopt $V_{\rm peak}$ (halo peak circular velocity) to perform SHAM. Both models account for fibre-collision effects, either in the measurements themselves (Saito et al. 2016) or in the model (Rodríguez-Torres et al. 2016). Importantly, the down-sampling procedure adopted in both studies assumes that CMASS galaxies are a random sample of the overall population at fixed stellar mass. However, Leauthaud et al. (2016) show that at fixed stellar mass, CMASS is not a random sample of the overall population in terms of galaxy colour. In short: both methodologies account for mass incompleteness but not for colour incompleteness. We will return to this point in Section 5.4.

4.2 Computation of predicted lensing signal from mocks

To compute the lensing signal predicted by CMASS mocks, we cross-correlate the positions of mock galaxies with the positions of dark matter particles to form the three-dimensional galaxy-mass cross-correlation function, $\xi_{\rm gm}$. To compute $\Delta\Sigma$ from $\xi_{\rm gm}$, we follow the equations outlined in section 4.2 of Leauthaud et al. (2011). Briefly, we begin by numerically integrating $\xi_{\rm gm}$ over the line of sight to form the projected surface mass density, Σ. In this step, it is important to perform the integral out to a large radii or else Σ will be underestimated. We find that integrating to 70–100 h^{-1} Mpc is sufficient for our purpose. Once we have computed Σ, we then compute $\Delta\Sigma$ via two additional integrals – details can be found in Leauthaud et al. (2011). We have verified that our code yields the same result as an independent derivation using the HALOTOOLS software package (Hearin et al. 2016). Finally, to account for the contribution of the stellar mass of the galaxy to the lensing signal, we add a point-source term to $\Delta\Sigma$ assuming a value of $\log(M_*) = 11.4$. This corresponds to the mean stellar mass of the CMASS sample as computed from the S82-MGC. In practice, this point source term only has a minor contribution to $\Delta\Sigma$ at $r < 100\ h^{-1}$ kpc.

4.3 Comparison between predicted and measured lensing signal

Fig. 7 displays our main result that is the comparison between the predictions from CMASS mocks and the measured lensing signal. All the predictions are drawn from mocks which have a volume that is larger than the volume corresponding to our lensing measurement. Hence, we neglect sampling errors on the mock predictions which should be subdominant compared to the errors on the measured lensing signal. The clustering measurements used to construct these mocks were derived from a larger area than the lensing (thousands of square degrees compared to a few hundred). Hence, any cross-covariance between the clustering and lensing should be negligible.

The first point to take away from Fig. 7 is that all the mocks yield a surprisingly similar prediction for $\Delta\Sigma$ with differences that are at most at the 20 per cent level (with most models agreeing at the 15 per cent level). This is quite remarkable given significant differences in the methodologies, cosmologies and *N*-body simulations used to construct the mocks. In addition, each mock was tuned to match a different set of observables – some reproduce the projected correlation function while others were tuned to fit the monopole or the quadrupole of the three dimensional redshift-space correlation function. We conclude from Fig. 7 that, under standard assumptions about how galaxies populate dark matter haloes, the clustering of CMASS makes a robust prediction for the amplitude of the lensing signal.

We now turn our attention to the comparison between the measured and the predicted lensing signal. Fig. 7 shows that *all the mock catalogues* predict a lensing amplitude that is larger by $\sim$20–40 per cent than our measurement. For example, the χ^2 between the measured lensing signal and the prediction from Saito et al. (2016) is $\chi^2/dof = 12.9$ with $dof = 13$. The χ^2 for the updated Saito et al. (2016) MDPL2 mock is $\chi^2/dof = 14.1$. The χ^2 difference with respect to other BOSS mocks have similar values.
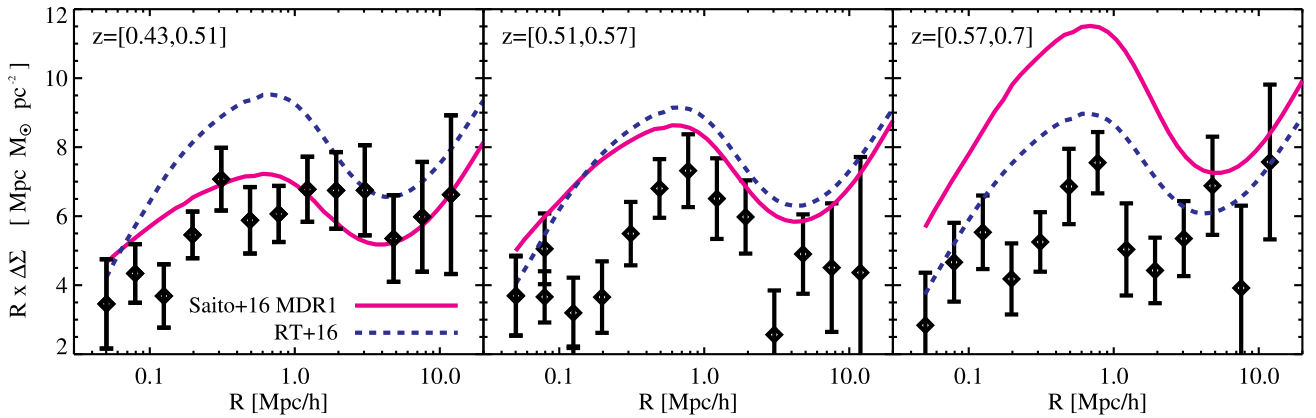
Figure 8. Redshift evolution of the CMASS g-g lensing signal compared to predictions from Saito et al. (2016) and Rodríguez-Torres et al. (2016). The Saito et al. (2016) model matches the lensing signal at low redshifts but then overpredicts the lensing signal at higher redshifts. The Rodríguez-Torres et al. (2016) model overpredicts the lensing signal by ~20–40 per cent at all redshifts.

Finally, we also investigate the redshift evolution of the CMASS g-g lensing signal. Fig. 8 displays the lensing signal for CMASS in three redshift bins compared to predictions from Saito et al. (2016) and Rodríguez-Torres et al. (2016). These results will be discussed in Section 5.3.

5 DISCUSSION

Our results demonstrate that standard models of the galaxy–halo connection tailored to reproduce the clustering of CMASS predict a g-g lensing signal that is 20–40 per cent higher than observed. We now discuss possible explanations for this mismatch. Because lensing measurements are non-trivial, systematic effects are a concern. However, we argue below that the observed difference is too large to be explained by lensing related systematics effects alone. This leads us to consider other explanations including the impact of a low value of σ_8, sample selection effects and assembly bias, the impact of baryons on the matter distribution, massive neutrinos and modified gravity effects.

5.1 Systematic effects

Could systematic effects explain the low amplitude of the lensing signal? Here, we summarize and discuss the dominant effects which could impact our measurement. Further details on the various tests that we have performed can be found in the Appendices.

Our dominant source of systematic uncertainty is associated with the photo-*z*s of source galaxies. If the photo-*z*s of source galaxies are biased, this may lead to a bias when evaluating the geometric factor $\Sigma_{\rm crit}$ (equation 3). How much would the photo-*z*s have to be wrong in order to explain Fig. 7? It is difficult to give a succinct answer to this question because $\Sigma_{\rm crit}$ responds non-linearly to z_S. However, to give an idea: when $z_L = 0.55$ a 30 per cent effect on $\Delta\Sigma$ requires a source at $z_S = 1$ to have a photo-*z* bias of $\Delta z = 0.16$. Fig. 1 that compares the photo-*z*s of source galaxies from CS82 with known spectroscopic redshifts, shows no evidence for a bias this large. Furthermore, Choi et al. (2016) have recently performed an analysis of the accuracy of the CFHTLenS photo-*z*s and found at most a bias of 0.049 in the photometric redshift bin spanning $0.57 < z_B < 0.7$ (in our case, most of our sources are removed from this range by our lens–source cuts). Finally, using a representative spectroscopic sample, we show in Appendix A2 that the impact of photo-*z* errors on $\Delta\Sigma$ are at the 3 per cent level (this estimate

includes the dilution of $\Delta\Sigma$ by source galaxies with $z_S^{\rm phot} > z_L$ but which are actually at redshifts below z_L). We conclude that photo-*z* bias alone is unlikely to explain Fig. 7.

It is common practice to apply a boost correction factor (see Appendix A2) to g-g lensing measurements to account for a dilution of the signal by physically associated sources. We have not applied this correction factor to our measurements for reasons that are outlined in Appendix A1. In short, we argue that a variety of effects (masking, deblending and failed photometry measurements in crowded regions) renders the computation of boost correction factors uncertain. Instead, we adopt a more empirical approach and show that our lensing signal is robust to lens–source separation cuts (see Appendix A2). This test is based on the following argument: if the lensing signal is subject to a large dilution factor, then we expect the amplitude of the signal to increase for more conservative source selections. The fact that our lensing signal is invariant for a range of lens–source separation cuts suggest that dilution caused by physically associated galaxies is not a large concern.

Another effect that we consider is that the weight function for CMASS is different between lensing and clustering measurements. Indeed, our predictions assume that lensing gives an equal weight to all haloes, but there are a variety of reasons (outlined in Appendix A5) why this may not be true. However, in Appendix A5 we show that the lensing signal is invariant even after removing the lensing specific weight function.

Finally, we consider the possibility of an unknown and unaccounted for bias in shear measurements from *lens*fit. This question is of particular importance because other surveys that use *lens*fit such as CFHTLenS and the KiDS (Kuijken et al. 2015) report lower amplitudes for cosmic shear measurements (e.g. Heymans et al. 2013; Hildebrandt et al. 2017) than predicted from Planck temperature fluctuations (Planck Collaboration XIII 2016). Tests with image simulations suggest that the multiplicative bias for *lens*fit is controlled to within a few per cent (Fenech Conti et al. 2016), but there is always the concern that shear calibration simulations may not be realistic enough. To address this concern, we measure the g-g lensing signal for a sample of massive low-redshift clusters from the redMaPPer cluster catalogue (v5.10, Rozo & Rykoff 2014; Rykoff et al. 2014) and compare with a fully independent measurement using the SDSS catalogue of Reyes et al. (2012). The shear calibration method for *lens*fit and for the Reyes et al. (2012) measurements are quite different: one uses simulations with galaxies

described by simple Sérsic profiles, while the other is based on simulations with realistic galaxy morphologies drawn from *Hubble Space Telescope* imaging. Appendix A6 shows that the mean inverse-variance-weighted offset between CS82 and SDSS is consistent with zero. Furthermore, Simet et al. (2017) have shown that lensing measurements from Reyes et al. (2012) agree with yet another fully independent shear catalogue referred to in their paper as the 'ESS' catalogue (e.g. Melchior et al. 2014; Clampitt & Jain 2015). The fact that three independent lensing measurements, with different shear calibration methods, yield the same results for $\Delta\Sigma$ suggest that a large bias in *lens*fit shear measurements is an unlikely possibility.

In conclusion, while lensing is a difficult measurement to make, we conservatively estimate that the fractional systematic error on $\Delta\Sigma$ is less than 5–10 per cent. The differences reported in Fig. 7 are thus too large to be explained by systematic effects alone.

5.2 Cosmology

The predictions in Fig. 7 are generated from *N*-body simulations with both WMAP and Planck-like cosmologies with Ω_m values that span the range 0.27–0.31. However, as can be seen from Table 2, the simulations used in our comparison only span the range $\sigma_8 = 0.82$–0.829. We now investigate how different σ_8 and Ω_m would have to be in order to explain the lensing signal.

So far, we have only considered model predictions derived directly from *N*-body simulations. There are two reasons for this. First, direct mock population provides a more robust theoretical prediction for our observables because, as opposed to analytic HOD type methods, there is no need to rely on analytical fitting functions for scale-dependent halo bias and halo exclusion. Secondly, as exemplified by Saito et al. (2016) and Rodríguez-Torres et al. (2016), the idiosyncrasies of the CMASS sample (e.g. redshift-dependent selection effects that lead to a redshift-dependent number density) can be directly folded into the modelling framework. The obvious downside of this approach, however, is that without resorting to sophisticated re-scaling (e.g. Angulo & Hilbert 2015) or emulator type techniques (e.g. Kwan et al. 2015), it is difficult to explore the cosmological dependences of our observables. For this reason, we now adopt an analytic HOD model to investigate the cosmological implications of these lensing measurements.

Because of sample selection effects, we do not expect a single redshift-independent HOD to capture the properties of CMASS (see fig. 10 in Saito et al. 2016). However, our goal here is not to provide precision cosmological constraints, but simply to gain an intuition for the impact of cosmological parameters on $\Delta\Sigma$, and for this, a simple redshift-independent HOD is sufficient. We use the analytical HOD modelling framework developed in van den Bosch et al. (2013) to perform a joint fit to $\Delta\Sigma$ and w_p^{CMASS} (see More et al. 2013, Cacciato et al. 2013 and More et al. 2015 for an application of this method to SDSS data). This analytical framework accounts for the radial dependence of halo bias, halo exclusion, residual RSDs in w_p^{CMASS} and the cosmological dependence of the measurements (More 2013). For modelling the CMASS sample, we use a simple five parameter description of the analytical HOD following Zheng, Coil & Zehavi (2007), and a nuisance parameter (see equation 67 in van den Bosch et al. 2013) that marginalizes over the uncertainty in the model predictions near the one- to two-halo transition regime. We assume that the matter density within haloes is described by an NFW profile with the concentration–mass relation of Macciò, Dutton & van den Bosch (2008). We also assume that the number of satellite galaxies within haloes of a given mass follows
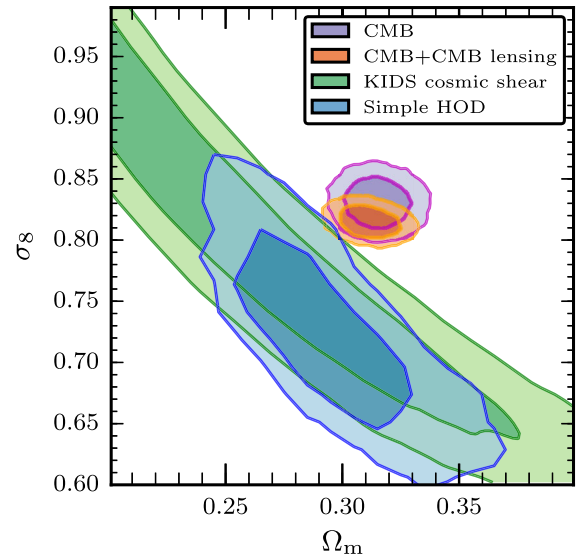

Figure 9. Blue contours represent the result of a joint HOD fit to the two point correlation function and the g-g lensing signal for CMASS galaxies where Ω_m and σ_8 are left as free parameters. The lensing amplitude can be matched by lowering the value of S_8 which reduces the halo masses of galaxies at fixed number density. Green contours represent contours from the KiDS cosmic shear analysis of Hildebrandt et al. (2017). Magenta contours show constraints from Planck Collaboration XIII (2016) and orange contours include the CMB lensing effect. Lowering the value of S_8 compared to Planck 2015 reconciles the lensing with clustering.

a Poisson distribution. Centrals are assumed to sit at the centre of dark matter haloes while the number density distribution within the halo follows the dark matter density.

Fig. 9 shows the contours on σ_8 and Ω_m from our joint HOD fit compared to constraints from Planck Collaboration XIII (2016).[16] We let Ω_m and σ_8 be completely free but use priors on the spectral index n_s, the Hubble parameter h, and the baryon density Ω_b, based the results of Hinshaw et al. (2013) which uses WMAP 9 yr data as well as high-resolution cosmic microwave background (CMB) measurements from the South Pole Telescope and the Atacama Cosmology Telescope. Lensing plus clustering constrains the parameter combination $S_8 = \sigma_8 \sqrt{\Omega_m/0.3}$. A 2σ–3σ change in S_8 compared to Planck 2015 is required in order to match the lensing amplitude just via changes in cosmological parameters. When combined with external data such as BOSS BAO, and within the context of ΛCDM, WMAP 9 yields similar values for S_8 as Planck 2015. Hence, this may indicate a more general tension between g-g lensing and the CMB. However, our measurements are dominated by highly non-linear scales, where other effects may also come into play (these will be discussed shortly), and so Fig. 9 should not be construed as direct evidence for a low value of S_8. None the less, Fig. 9 does become more interesting when considered in the context of other independent constraints on the amplitude of low-redshift structure, both from lensing and from cluster abundances (e.g. Cacciato et al. 2009, 2013; Heymans et al. 2013; MacCrann et al. 2015; Giannantonio et al. 2016; Planck Collaboration XXIV 2016; Hildebrandt et al. 2017; Joudaki et al. 2017), that yield lower σ_8 values compared to Planck 2015 (but also see Jee et al. 2013 and

---

[16] Specifically, we use Planck constraints that use both temperature and polarization data (Planck chain 'plikHM_TTTEEE_lowTEB') as well as lensing of the CMB (Planck chain 'plikHM_TTTEEE_lowTEB_lensing').

The Dark Energy Survey Collaboration et al. 2016 for cosmic shear results consistent with Planck 2015).

In particular, the analysis of Cacciato et al. (2013) most closely resembles the ones presented here. Cacciato et al. (2013) performed a joint analysis of the abundance, clustering and the g-g lensing signal of the SDSS main sample and found results which were consistent with WMAP 7 yr results, although with a preference for a lower value for σ_8. The discrepancy was exacerbated when compared to the CMB constraints from Planck (see fig. 11 in More et al. 2015). In contrast, the cosmological constraints from More et al. (2015) show considerable overlap with the Planck constraints given the clustering and lensing signal of a subsample of CMASS. However, they have used a more flexible HOD, which includes a parametric form to model incompleteness, miscentring of galaxies (or missing central galaxies with the CMASS selection criteria), and differences in galaxy and dark matter concentrations. Although such effects cannot be ruled out, this more flexible HOD leads to inflated inferred errors on cosmological constraints and thus may be hiding the discrepancy. We argue that characterizing and including sample selection effects into the modelling framework (e.g. Rodríguez-Torres et al. 2016; Saito et al. 2016) is a more robust approach.

To summarize: lowering the value of S_8 by 2σ–3σ compared to Planck 2015 reconciles the lensing with clustering. However, as argued in the following sections, at this level of precision, there are other effects that also come into play that need to be taken into consideration and disentangling these effects is a non-trivial challenge.

5.3 Sample selection effects

On the relatively small radial scales considered here, the comparison between lensing and clustering is sensitive to the details of exactly how galaxies occupy dark matter haloes. We now turn our attention to galaxy formation related explanations for the low lensing amplitude.

The lack of redshift evolution of the lensing signal may contain important clues. The CMASS sample is not a single homogenous population and has properties that vary with redshift. According to the s82MGC, the mean stellar mass of CMASS increases by a factor of 1.8 over the range $0.43 < z < 0.7$. Based on the SHAM modelling of Saito et al. (2016), this should lead to a factor of 3.5 increase in the predicted mean halo mass[17] of CMASS from $z = 0.43$ to $z = 0.7$ (see fig. 12 in Saito et al. 2016). This prediction stands in sharp contrast with the lack of redshift evolution in the CMASS lensing signal[18] displayed in Fig. 10 and indicates that the models are an insufficient description of the data. One possible explanation for Fig. 10 is that the mean stellar mass of CMASS evolves less strongly with redshift than predicted by the s82MGC. For example, it is possible that the luminosity estimates from the s82MGC have a redshift-dependent bias because they do not fully capture light at the outskirts of galaxies. This type of bias could depend on galaxy type. New deep surveys such as HSC will yield better estimates for the total luminosities of massive galaxies and will shed light on this question (Huang et al., in preparation).
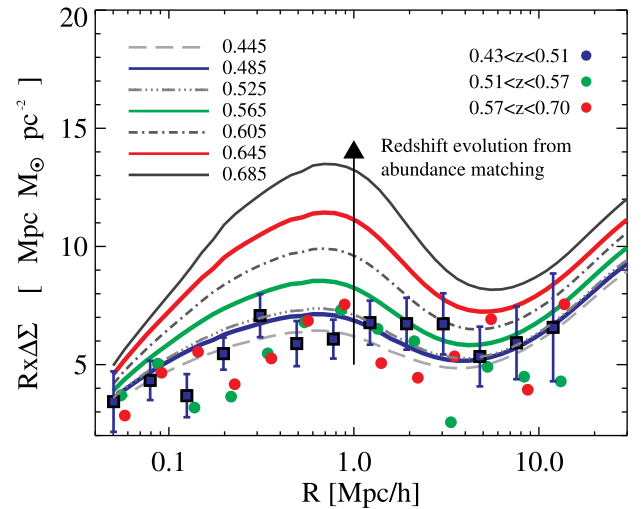

Figure 10. Predicted redshift evolution of the lensing signal from the abundance matching model of Saito et al. (2016) compared to the measured lensing amplitude in three redshift bins. According to the s82MGC, the mean stellar mass of the CMASS sample increases by a factor of 1.8 over the range $0.43 < z < 0.7$. As a consequence, SHAM predicts that the mean halo mass should increase by a factor of 3.5 from low to high redshift.

Another important point is that although some of the mocks discussed so far account for the stellar mass completeness of the sample, none account for colour completeness *in addition* to mass completeness. The colour cuts that define CMASS exclude galaxies at low redshift with recent star formation. At higher redshifts ($z > 0.6$), the sample is mainly flux limited and includes a larger range of galaxy colours at fixed magnitude (see fig. 5 in Leauthaud et al. 2016). A range of studies suggest that at fixed stellar mass, galaxies with different levels of star formation live in haloes of different mass. At low redshift, studies find that at fixed stellar mass, blue central galaxies live in lower mass haloes (e.g. Mandelbaum et al. 2016, and references therein). At higher redshift, there are suggestions that this trend may reverse (Tinker et al. 2013). A possible explanation of Fig. 10 is that the inclusion of more blue galaxies in the CMASS sample at higher redshifts leads to a coincidental compensation that keeps the amplitude of the lensing fixed. However, although this may explain the lack of evolution in the lensing – this does not immediately explain why the predicted lensing signal is lower than observed unless CMASS galaxies occupy haloes in a way that leads to an unusual[19] relation between the mass of their dark matter haloes and their large-scale clustering properties. For example, assembly bias may be at play and is discussed in the next section.

5.4 Assembly bias effects

The model predictions shown in Fig. 7 use standard galaxy–halo modelling based on either HOD or SHAM type methodologies. The fact that the amplitude of the lensing does not match the predictions from these models may reflect an inherent failure of such models. In particular, as highlighted by Zentner, Hearin & van den Bosch (2014), one aspect that has recently come to the forefront is that these models[20] neglect assembly bias: the fact that in

---

[17] The redshift range of CMASS only corresponds to a time span of 2 Gyr and we do not expect much intrinsic evolution in the global connection between galaxy mass and halo mass over such a short timeframe.

[18] The clustering of CMASS is also constant with redshift. See fig. A1 in Reid et al. (2014) and fig. 12 in Saito et al. (2016).

[19] Unusual here means unlike the range of models considered in Fig. 7.

[20] Standard HOD models have no assembly bias, whereas SHAM models based on V_{peak} do have some levels of assembly bias (Zentner et al. 2014).
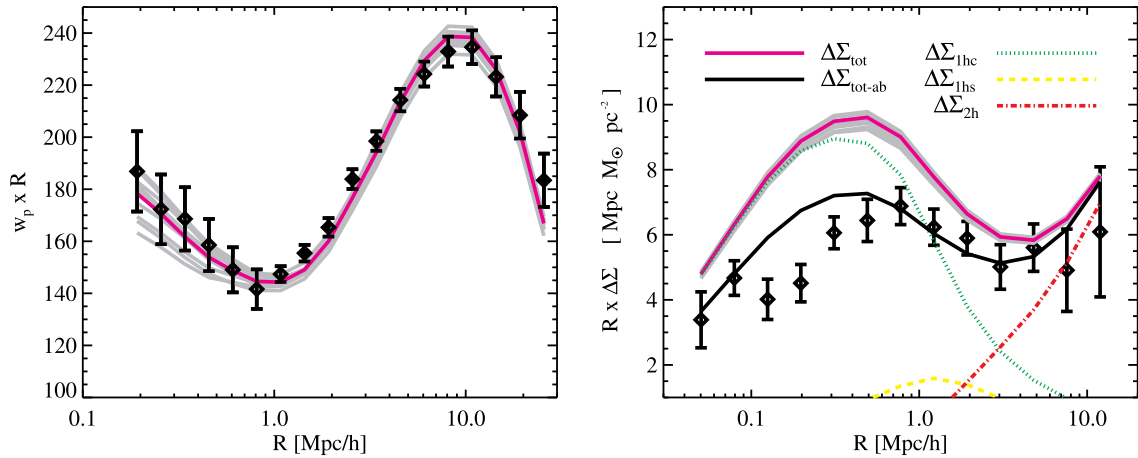
Figure 11. Right-hand panel: a simple four parameter HOD fit to w_p^{CMASS} at fixed cosmology. Grey lines represent models drawn from the 68 per cent confidence region. Right-hand panel: predicted lensing signal (solid magenta line). Grey lines represent models drawn from the 68 per cent confidence region of the best-fitting to w_p^{CMASS}. The lensing signal can be decomposed into a one-halo central term (green dotted line), a one-halo satellite term (dashed yellow line), and a two-halo term (red dash–dotted line). The satellite fraction for CMASS is only of the order of ~ 10 per cent and the one-halo satellite term is therefore subdominant on all scales. The black solid line is the total lensing signal obtained by lowering $\Delta\Sigma_{1hc}$ by 25 per cent, which roughly corresponds to lowering the halo mass by 35 per cent while keeping the bias fixed.

addition to halo mass, the strength of halo clustering depends on other properties such as halo age, spin and concentration (Gao, Springel & White 2005; Wechsler et al. 2006; Gao & White 2007; Zentner 2007; Dalal et al. 2008; Lacerna & Padilla 2011). Although assembly bias is manifest in dark matter simulations, we do not know if it is also manifest in the clustering of galaxies. Recent observational evidence suggests the possibility of assembly bias in galaxy and cluster samples (Miyatake et al. 2016; More et al. 2016; Zentner et al. 2016; Lehmann et al. 2017), but these detections are not without challenges (Paranjape et al. 2015; Lin et al. 2016).

If galaxy formation processes are sensitive to halo parameters besides halo mass, for example, if the ages of galaxies correlate with the ages of their dark matter haloes, then assembly bias effects will be more pronounced for colour-selected samples such as CMASS. The clustering of CMASS tightly constrains the large-scale bias of the sample. However, the lensing signal that we measure is limited to $r < 10\ h^{-1}$ Mpc and is primarily sensitive to the one-halo term and the mean halo mass of the sample. Hence, the difference that we observe may suggest a tension between the halo mass and the large-scale bias of this sample – the smoking gun for assembly bias. This interpretation would mean that CMASS host haloes are not a representative sample of all dark matter haloes at the same mass, and since the bias of haloes depends on other properties apart from their mass, they thus show a different clustering amplitude than such a representative sample.

In Saito et al. (2016), we present the first analysis of the effects of assembly bias on the clustering properties of CMASS. However, our analysis assumed a simplified model for the colour completeness of CMASS. To build on Saito et al. (2016), the next step would be to characterize the colour-completeness of CMASS and to explore the impact of assembly bias using, for example, conditional SHAM techniques (e.g. Hearin et al. 2014). This type of in-depth analysis is beyond the scope of this paper. Instead, we present a simple first-order computation to determine if assembly bias is a plausible explanation for the observed offset. We fit a simple four parameter HOD to w_p^{CMASS} (details are given in Appendix A7) and show the results in Fig. 11. The predicted lensing signal can be decomposed into three components: the one-halo central term ($\Delta\Sigma_{1hc}$), the one-halo satellite term ($\Delta\Sigma_{1hs}$) and the two-halo term ($\Delta\Sigma_{2h}$). Fig. 11

shows that the amplitude of the lensing signal is well matched if the one-halo central term is decreased by 25 per cent while keeping the two-halo term fixed.[21] In this regime, $M_{\mathrm{halo}} \propto (\Delta\Sigma_{1hc})^{3/2}$ so this corresponds to a ~ 35 per cent decrease in halo mass. The halo masses of CMASS galaxies are firmly above collapse mass at $z = 0.55$ (Saito et al. 2016) where the effects of assembly bias are complex[22] and not yet necessarily well characterized. With this caveat in mind, assembly bias can plausibly explain a ~ 35 per cent decrease in halo mass at fixed bias (see fig. 4 in Li et al. 2008 for example). Lensing measurements on larger radial scales will be extremely valuable for testing this hypothesis.

If assembly bias is at play, this could have implications for the growth of structure constraints from RSDs (Alam et al. 2017, and references therein). Unlike BAO measurements, RSD methods push into the semi-non-linear regime and need to be validated against using mock catalogues. Current tests suggest that RSD methods are robust to the details of galaxy formation (see section 7.2 in Alam et al. 2017), but the full range of galaxy formation models has yet to be tested, and hence the theoretical systematic associated with the complexities of galaxy bias is unknown. Assembly bias and the details of the galaxy–halo connection may become an important systematic effect for RSD constraints from upcoming surveys such as DESI (Levi et al. 2013). Lensing measurements such as presented in this paper will play an important role in characterizing these effects.

5.5 Baryon effects

The BOSS CMASS mock catalogues used for computing the model predictions are based on gravity-only N-body simulations, which do not account for possible effects of baryon physics processes on the matter distribution. However, baryon physics processes can affect the matter profiles of haloes and also influence the properties

---

[21] This exercise is simplistic because it does not necessarily preserve the CMASS clustering or abundance.

[22] The magnitude and sign of assembly bias effects above collapse mass depends sensitively on the definition of halo age (e.g. Li, Mo & Gao 2008).
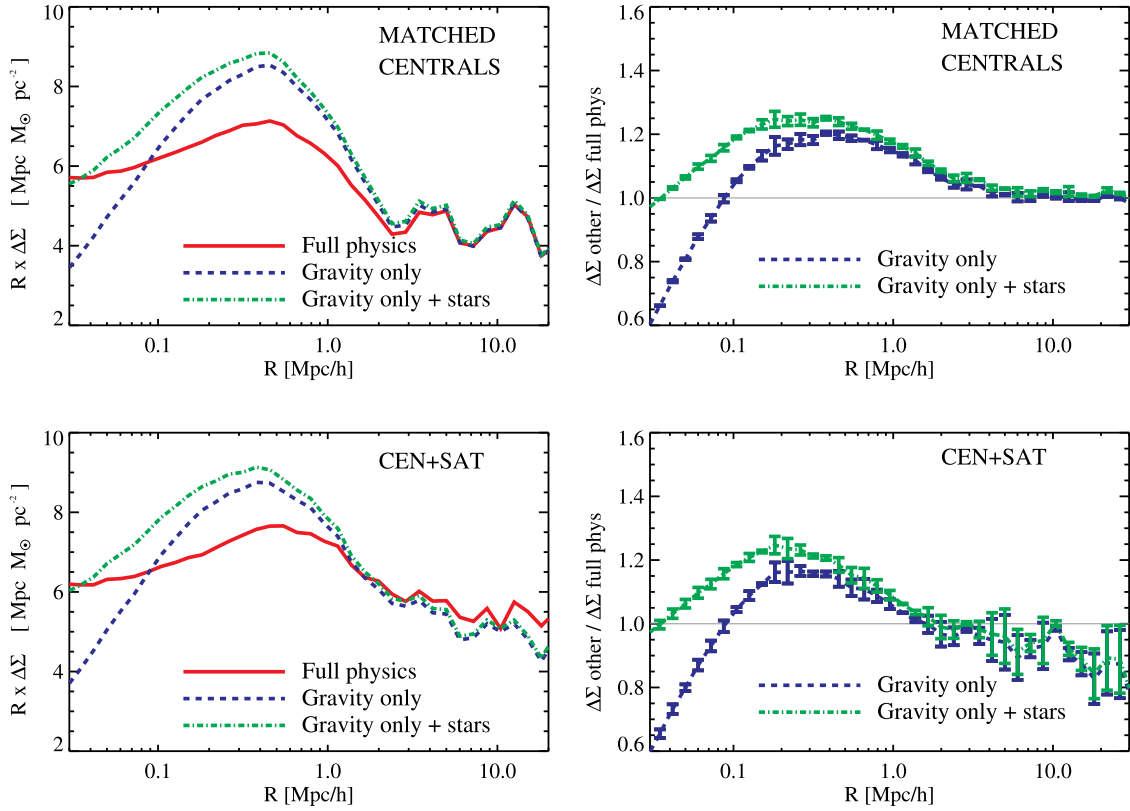
Figure 12. Left-hand panels: comparison of $\Delta\Sigma$ for massive galaxies with CMASS-like number densities for the gravity-only Illustris-1-Dark run (blue dashed line) and the full-physics Illustris-1 run (solid red line). The green dash–dotted line shows $\Delta\Sigma$ for the gravity-only run plus the stellar component from the full-physics run. Right-hand panels: ratio of $\Delta\Sigma$ from the gravity-only run and from the full-physics run (blue line). The green dash–dotted line shows the result including the contributions from stars. The error bars indicate the spread between the ratios obtained from using the three different principal simulation box axes as viewing direction. Upper panels: fixed number density selection for matched centrals. Lower panels: fixed number density selection including both centrals and satellites.

of subhaloes (e.g. van Daalen et al. 2014; Velliscig et al. 2014; Chaves-Montero et al. 2016).

We use the Illustris simulations (Genel et al. 2014; Vogelsberger et al. 2014a,b; Nelson et al. 2015; Sijacki et al. 2015) to estimate the impact of baryonic effects for CMASS-like samples. We compare results from snapshots at redshift $z = 0.5$ of the full-physics Illustris-1 simulation and of the corresponding gravity-only Illustris-1-Dark simulation with matched initial conditions. The Illustris simulation corresponds to a comoving volume of $(75\,h^{-1}\,\mathrm{Mpc})^3$ which means that there will be considerable sample variance uncertainties associated with galaxy selections at these number densities. Our goal here, however, is not to compare directly with the BOSS measurements, but simply to estimate relative differences between the full-physics and gravity-only runs.

We rank order subhaloes in both simulations according to their maximum circular velocity, V_{max}, and apply a sharp lower limit on V_{max} to select samples with number densities of $\bar{n} = 4 \times 10^{-4}(h^{-1}\,\mathrm{Mpc})^{-3}$. The resulting lower limit is $V_{max} = 351\,\mathrm{km\,s^{-1}}$ for the gravity-only run, and $V_{max} = 367\,\mathrm{km\,s^{-1}}$ for the full-physics run. This selection results in 170 galaxies.[23] In addition to this sample which includes all subhaloes, we also perform a number density

selection which includes only *matched parent* haloes. $\Delta\Sigma$ is computed for all samples using each of the three principal box axes as a viewing direction using fast Fourier transform methods (Hilbert, Hartlap & Schneider 2011; Hilbert et al. 2016). Finally, $\Delta\Sigma$ is also computed from the gravity-only run with an added contribution from the stellar component computed from the full-physics run. The resulting weak-lensing profiles are shown in Fig. 12.

The upper panel in Fig. 12 shows the impact of baryons on $\Delta\Sigma$ for matched parent haloes with $\bar{n} = 4 \times 10^{-4}(h^{-1}\,\mathrm{Mpc})^{-3}$. For small separations ($R < 0.1\,h^{-1}\,\mathrm{Mpc}$), $\Delta\Sigma$ is larger in the full-physics simulation than in the gravity-only simulation. This is mainly due to the contribution from stars, which are missing in the gravity-only run. On intermediate scales, $\Delta\Sigma$ is larger in the gravity-only run than in the full-physics run by up to 20 per cent. This is due to feedback processes in the full-physics simulation that drive matter out of the inner parts of haloes. These feedback processes also lower the baryon fraction in the haloes and decrease the matter power spectra on these scales (Vogelsberger et al. 2014a). However, $\Delta\Sigma$ converges on larger scales ($R > 4\,h^{-1}\,\mathrm{Mpc}$), indicating that the impact of baryons for central haloes is primarily limited to the one-halo regime.

The lower panels in Fig. 12 show $\Delta\Sigma$ for a fixed number density selection including all subhaloes. The main difference with respect to the matched-parent sample is now that on large scales $\Delta\Sigma$ is higher in the full-physics run than in the gravity-only run. This is because the full-physics run has a larger satellite fraction ($f_{sat} = 22$ per cent compared to 11 per cent in the gravity-only

---

[23] With only 170 subhaloes with $V_{max} = 351\,\mathrm{km\,s^{-1}}$, the Illustris simulation is not large enough to compute the clustering signal for galaxies at these low number densities. Our tests are therefore based on a simple number density selection without also matching the clustering.

run), and these satellites live is massive host haloes. The larger fraction of satellites (and subhaloes with large V_{max}) is probably because satellites are more resistant to tidal stripping and are able to survive longer in the full-physics run.[24] This factor of 2 difference in the satellite fraction between the full-physics run and the gravity-only run is particularly interesting because w_p^{CMASS} is very sensitive to this quantity. For example, the error on the CMASS satellite fraction from Reid et al. (2014) is less than 1 per cent![25] If these constraints are robust, they could be very informative for feedback models. However, given the tensions with respect to the lensing, it is not clear if these HOD constraints on the CMASS satellite fraction are indeed robust. What is clear, however, is that a factor of 2 difference in the satellite fraction will have a large impact on CMASS abundance matching models which are currently based on gravity-only N-body simulations. Analytic HOD models may be able to marginalize over baryonic effects by allowing the concentration of the satellite distribution and the concentration of the parent dark matter halo to vary as free parameters (e.g. van den Bosch et al. 2013; Reddick et al. 2014). But current implementations of SHAM, and HOD models based on direct N-body mock population, do not have this flexibility.

The tests presented here suggest that baryonic effects can induce a 10–30 per cent difference in $\Delta\Sigma$[26] (with a characteristic scale dependence) and a factor of 2 difference in the satellite fraction for galaxy samples with $\bar{n} = 4 \times 10^{-4}$ $(h^{-1}\,\mathrm{Mpc})^{-3}$. This level of difference is no longer negligible given the statistical errors on our measurements. Without further analysis, it is difficult to say exactly how these effects would play out in an HOD or SHAM analysis of the clustering of BOSS galaxies, and whether or not the differences go in the same direction as our lensing measurements. However, it is clear that these effects warrant further investigation.

5.6 Effect of massive neutrinos

The total sum of neutrino masses is tightly constrained by cosmological observations to $\sum m_\nu < 0.1$–0.5 eV (e.g. Saito, Takada & Taruya 2011; Zhao et al. 2013; Beutler et al. 2014; Palanque-Delabrouille et al. 2015; Alam et al. 2017). Finite-mass neutrinos have large velocity dispersion and suppress the growth of LSS below the neutrino free-streaming scale (e.g. Lesgourgues & Pastor 2006; Saito, Takada & Taruya 2008, 2009) and could therefore impact the amplitude of the g-g lensing signal. Here we make a simple attempt to quantify the impact of neutrino masses on the g-g lensing signal (see also Mandelbaum et al. 2013 and More et al. 2013). We run three N-body simulations using the particle-based method of Villaescusa-Navarro et al. (2014) with initial conditions generated following Zennaro et al. (2017). The three simulations share the

[24] Determining the subhalo fraction is a difficult task because simulations that lack resolution may result in artificial subhalo disruption. We raise this as a caveat to the numbers presented here, but have not explored these aspects further.

[25] Our Illustris tests are performed using a simple fixed number density cut and are hence only a very loose approximation of the CMASS sample. Without a more careful attempt to match the stellar mass distribution of CMASS, the Reid et al. (2014) constraint on f_{sat} (10.16 ± 0.69 per cent) should not be directly compared with the values quoted for our Illustris sample.

[26] As we were finishing this paper, new simulations from the Illustris group with an improved AGN feedback model suggest a smaller impact of baryonic effects on halo masses (Weinberger et al. 2017).
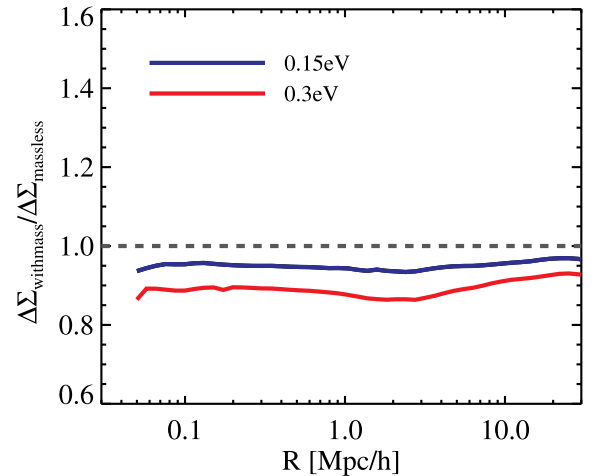

Figure 13. Ratio of $\Delta\Sigma$ from simulations with massive neutrinos to $\Delta\Sigma$ from simulations with massless neutrinos. The blue corresponds to $\sum m_\nu = 0.15$ eV and the red line corresponds to $\sum m_\nu = 0.3$ eV. The impact of massive neutrinos leads a fairly scale independent decrease of $\Delta\Sigma$ over the scales of interest that could partially alleviate the tension reported in this paper.

same initial seeds and have the same value for the total matter density ($\Omega_m = \Omega_{CDM} + \Omega_b + \Omega_\nu = 0.3175$) but have different neutrino masses (0, 0.15 and 0.3 eV). Our N-body simulations are created using GADGET-3 (Springel, Di Matteo & Hernquist 2005) with parameters $L_{box} = 300\,\mathrm{Mpc}\,h^{-1}$, $N_{CDM} = 512^3$ and $N_\nu = 512^3$ (for the non-zero neutrino mass simulations). Subhaloes are identified using the SUBFIND algorithm (Springel et al. 2001; Dolag et al. 2009) and a CMASS-like sample is selected via a simple constant number density cut with $\bar{n} = 3 \times 10^{-4}$ $(h/\mathrm{Mpc})^3$ after rank-ordering subhaloes by V_{max}.

Fig. 13 shows the impact of massive neutrinos on $\Delta\Sigma$. A larger neutrino mass results in a lower amplitude for $\Delta\Sigma$, but only affects the signal at the ∼10 per cent level even with 0.3 eV. This suppression is expected because massive neutrinos alter the halo mass function and globally reduce halo masses (Ichiki & Takada 2012; Castorina et al. 2014, 2015). Indeed, the mean halo masses for the three samples are $\log_{10} \overline{M}_{vir} = 13.60$, 13.55 and 13.51 for the 0, 0.15 and 0.3 eV simulations, respectively. Finally, we also find that the satellite fractions and the galaxy–galaxy correlation function are very similar among the three simulations. This is also expected because neutrinos only have a small impact on physics in the one-halo regime and the difference in the one-halo regime is mainly driven by differences in σ_8 (Fontanot et al. 2015).

We conclude from Fig. 13 that the effect of massive neutrinos goes in the right direction to explain the low amplitude of our lensing signal. However, the impact of massive neutrinos on $\Delta\Sigma$ is at the ∼10 per cent level at most, and so massive neutrinos alone are unlikely to be the full story.

5.7 Modified gravity effects

Observations of RSDs provide an exciting opportunity to constrain models of modified gravity (Zhang et al. 2007; Reyes et al. 2010; Samushia et al. 2013). In particular, one promising method is to examine the velocity structure around massive clusters with halo masses determined via weak lensing (Schmidt 2010; Lam et al. 2012; Lombriser et al. 2012; Zu et al. 2014). If GR is valid, then the phase space around clusters is uniquely determined by the mass
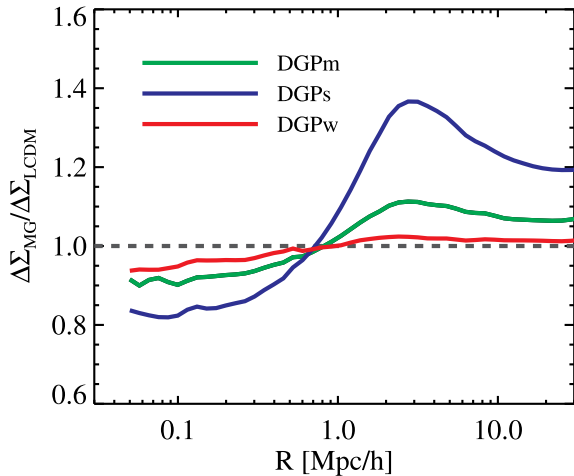
Figure 14. Ratio of $\Delta\Sigma$ from DGP gravity simulations and $\Delta\Sigma$ from ΛCDM. The three curves show the result for varying strength of the modified gravity effects, with DGPs, DGPm and DGPw corresponding to strong, medium and weak departures from GR, respectively. When the galaxy clustering strength is held fixed, departures from GR leave a scale-dependent signature in $\Delta\Sigma$.

of the clusters that source these velocities (but see Hearin 2015 for caveats due to assembly bias effects). Although the CMASS sample is more complex than a simple cluster selection (which means that this test can only be carried out in tandem with the modelling of the CMASS–halo connection), differences between the lensing and predictions from models trained on the two-dimensional redshift-space correlation function (Reid et al. 2014; Rodríguez-Torres et al. 2016) could be a signature of modified gravity. However, it is not immediately clear if deviations from GR would result in an *increase* or a *decrease* of the lensing amplitude.

To investigate this question, we use a suite of four $z = 0.57$ CMASS mock catalogues from Barreira, Sánchez & Schmidt (2016). One of these mocks is a ΛCDM control sample. The three other mocks are built from simulations (with $L_{box} = 600 \, h^{-1}$ Mpc and $N_p = 1024^3$) of structure growth for the normal branch of the Dvali–Gabadadze–Porrati gravity model (DGP; Dvali, Gabadadze & Porrati 2000) which were created using the ECOSMOG N-body code (Li et al. 2012; Li, Zhao & Koyama 2013). The three DGP gravity mocks simulate strong, medium and weak departures from GR and will be referred to, respectively, as 'DGPs', 'DGPm' and 'DGPw'. The expansion rate in these simulations matches the ΛCDM control simulation which means that any differences compared to ΛCDM are induced by modifications to the gravitational force law (Schmidt 2009). CMASS mocks were created using an HOD model with parameters tuned to roughly match the CMASS number density and the large-scale amplitude of the CMASS power spectrum monopole. While these mocks were not designed to reproduce the clustering of CMASS as accurately as those used in Fig. 7, they are still useful to understand the relative effects on $\Delta\Sigma$ for DGP-like models. Fig. 14 shows the lensing signals of the DGP and ΛCDM CMASS mock samples. We find that DGP gravity leaves a scale-dependent signature in $\Delta\Sigma$ with a transition region located at $r \sim 1 \, h^{-1}$ Mpc. There are at least two relevant effects responsible for the difference between the DGP results and ΛCDM which are now discussed.

The first effect is due to the existence of a positive additional 'fifth' force in the DGP simulation which is common feature in many modified gravity models (e.g. Joyce, Lombriser & Schmidt 2016).

At fixed halo mass, the fifth force favours the pileup and clustering of matter close to the accretion region of dark matter haloes ($r > 1 \, h^{-1}$ Mpc) which leads to a boost in the amplitude of the lensing signal. On smaller scales ($r < 1 \, h^{-1}$ Mpc), the effects of the fifth force on matter clustering tend to become less pronounced because of the efficient Vainshtein[27] suppression.

The second effect is that the distribution of halo masses differs between the DGP and the ΛCDM mock. Fig. 3 of Barreira et al. (2016) shows that mock CMASS galaxies live in lower mass haloes with increasing fifth force strength. These differences in the HOD models arise to preserve the galaxy number density and large-scale amplitude of the power spectrum monopole given modified halo abundances, halo bias and linear matter power spectrum. Because the DGP mocks contain more low-mass haloes, the amplitude of the lensing signal is suppressed relative to ΛCDM.

Overall, Fig. 14 shows that these two competing effects result in a difference to $\Delta\Sigma$ that is scale dependent, reflecting the regimes where each of these two effects dominate. Of the three DGP cases shown, the DGPs and DGPm ones are those which have the largest impact on $\Delta\Sigma$. However, these two particular models are already severely disfavoured by current growth rate measurements (Barreira et al. 2016). The DGPw case has a goodness-of-fit to the growth rate data that is comparable to ΛCDM, but its impact on $\Delta\Sigma$ does not exceed 5 per cent, thereby falling short of the 30 per cent mismatch displayed in Fig. 7. Furthermore, the DGP gravity models that we have explored predict a scale dependence in the lensing amplitude, which is inconsistent with our observations which suggest a fairly scale-independent offset. These tests suggest that the mismatch between the ΛCDM mocks and data in Fig. 7 is unlikely to be solely explained by DGP-like modifications to gravity, or other theories with similar phenomenology.

6 SUMMARY AND CONCLUSIONS

We report high-signal-to-noise g-g lensing measurements ($S/N = 30$) for the BOSS CMASS sample of massive galaxies at $z \sim 0.55$ using 250 deg^2 of weak-lensing data from the CFHTLenS and CS82 surveys. We compare the amplitude of this signal with predictions from mock catalogues trained to match a variety of observables including the galaxy SMF, the projected correlation function, and the two-dimensional redshift space clustering of CMASS. All models yield surprisingly similar prediction for the lensing observable $\Delta\Sigma$ with differences that are at the 20 per cent level at most (with most models agreeing at the 15 per cent level). This is quite remarkable given significant differences in the methodologies (including both HOD and SHAM), cosmologies, and N-body simulations that were used to construct the models. We conclude that given standard assumptions about how galaxies populate dark matter haloes, the clustering of CMASS makes a robust prediction for the amplitude of the lensing signal.

Fig. 7 corresponds to our main result which is the comparison between model predictions and the lensing measurement. This comparison reveals that the amplitude of the CMASS g-g lensing signal is 20–40 per cent lower than predicted from standard models of the galaxy–halo connection constrained by the clustering of CMASS.

---

[27] The term 'Vainshtein screening' denotes a non-linear effect that is at play in the DGP model and that dynamically suppresses the size of the modifications to gravity in regions where the enclosed matter density is large.

We present a detailed investigation of a range of systematic effects associated with lensing measurements, including the effects of photo-z errors, boost factors and the effects of the lensing weight function. Our measurement is robust to all of these effects. Furthermore, our CS82 lensing catalogue yields the same values for $\Delta\Sigma$ as an independent lensing measurements from SDSS. Our tests (the details of which are mostly given in the appendices) show that the differences reported in Fig. 7 are too large to be explained by systematic effects alone and that the mismatch is a genuine effect.

This leads us to consider other explanations for the low lensing amplitude. The combination of g-g lensing and clustering is sensitive to $S_8 = \sigma_8\sqrt{\Omega_m/0.3}$. We use an analytic HOD formalism to perform a joint fit to $\Delta\Sigma$ and to w_p^{CMASS} where σ_8 and Ω_m are left as free parameters. Fig. 9 shows that lowering the value of S_8 by 2σ–3σ compared to Planck 2015 reconciles the lensing with clustering. Because our measurements are dominated by non-linear scales where the details of the galaxy–halo connection matter, these results alone should not be construed as evidence for a low value of S_8. However, the cosmological interpretation of these results does become more interesting when considered in the context of multiple constraints on the amplitude of low-redshift structure, both from lensing and from cluster abundances (e.g. Cacciato et al. 2009, 2013; Heymans et al. 2013; Planck Collaboration XXIV 2016; Hildebrandt et al. 2017; Joudaki et al. 2017), that yield lower amplitudes compared to the Planck 2015 ΛCDM predictions (but also see Jee et al. 2013, The Dark Energy Survey Collaboration et al. 2016).

The model predictions shown in Fig. 7 use standard galaxy–halo modelling based on either HOD or SHAM type methodologies. The fact that the amplitude of the lensing does not match the predictions from these models may reflect an inherent failure of such models. If the ages of galaxies correlate with the ages of their dark matter haloes, then assembly bias effects may be present in colour selected samples such as CMASS. The clustering of CMASS tightly constrains the large-scale bias of the sample whereas the lensing is sensitive to the mean halo mass. The difference that we observe may suggest a tension between the halo mass and the large-scale bias of this sample – the smoking gun for assembly bias. If assembly bias is at play, it could be a systematic effect for RSD constraints from upcoming surveys such as DESI (Levi et al. 2013). Lensing measurements such as presented in this paper can play an important role in understanding theoretical systematic uncertainties associated with the complexities of galaxy bias.

Another effect that may be non-negligible given the precision of our measurements is the impact of baryon physics processes on the matter distribution. We use the Illustris simulations to present a first estimate of the magnitude of baryonic effects on the weak-lensing profiles of subhalo-abundance matched galaxies at BOSS CMASS-like number densities and redshifts. We find that baryonic effects can induce a 10–30 per cent difference in $\Delta\Sigma$ (with a characteristic scale-dependence) and a factor of 2 difference in the satellite fraction for CMASS-like galaxy samples. This level of difference is no longer negligible given the statistical errors on our measurements. Without further analysis, it is difficult to say exactly how these effects would play out in an HOD or SHAM analysis of the clustering of BOSS galaxies, and whether or not the differences go in the same direction as our lensing measurements.

We also consider the impact of finite mass neutrinos on $\Delta\Sigma$. We run three N-body simulations with the same value for the total matter density but with different neutrino masses (0, 0.15 and 0.3 eV). We show that the effect of massive neutrinos goes in the right direction to explain the low amplitude of our lensing signal. However, the impact of massive neutrinos on $\Delta\Sigma$ is at the ~10 per cent level

at most, and so massive neutrinos alone are unlikely to be the full story.

Finally, we investigate the impact of modified gravity on $\Delta\Sigma$ and show that the existence of a positive additional 'fifth' force common to many modified gravity models leaves a scale-dependent signature in the lensing signal. The amplitude of this effect, combined with the fact that our reported difference is fairly scale independent, leads us to conclude that modified gravity effects are unlikely to explain the difference reported in this paper.

The mismatch that we report could be due to one, or a combination of the effects described above. Disentangling cosmological effects from the details of the galaxy–halo connection, the effects of baryons, and finite mass neutrinos, is the next challenge facing joint lensing and clustering analyses. This is especially true in the context of large galaxy samples from BAO surveys with precise measurements but complex selection functions.

REFERENCES

Abazajian K. N. et al., 2009, ApJS, 182, 543
Ahn C. P. et al., 2014, ApJS, 211, 17
Aihara H. et al., 2011, ApJS, 193, 29
Alam S. et al., 2015, ApJS, 219, 12
Alam S., Miyatake H., More S., Ho S., Mandelbaum R., 2017, MNRAS, 465, 4853
Anderson L. et al., 2012, MNRAS, 427, 3435
Anderson L. et al., 2014, MNRAS, 441, 24
Angulo R. E., Hilbert S., 2015, MNRAS, 448, 364
Annis J. et al., 2014, ApJ, 794, 120
Applegate D. E. et al., 2014, MNRAS, 439, 48
Barreira A., Sánchez A. G., Schmidt F., 2016, Phys. Rev. D, 94, 084022
Behroozi P. S., Conroy C., Wechsler R. H., 2010, ApJ, 717, 379
Benítez N., 2000, ApJ, 536, 571
Benjamin J. et al., 2013, MNRAS, 431, 1547
Berlind A. A., Weinberg D. H., 2002, ApJ, 575, 587
Beutler F. et al., 2014, MNRAS, 444, 3501
Blake C. et al., 2016, MNRAS, 456, 2806
Bolton A. S. et al., 2012, AJ, 144, 144
Boulade O. et al., 2003, in Iye M., Moorwood A. F. M., eds, Proc. SPIE Conf. Ser. Vol. 4841, Instrument Design and Performance for Optical/Infrared Ground-based Telescopes. SPIE, Bellingham, p. 72
Brainerd T. G., Blandford R. D., Smail I., 1996, ApJ, 466, 623
Bundy K. et al., 2015, ApJS, 221, 15
Cacciato M., van den Bosch F. C., More S., Li R., Mo H. J., Yang X., 2009, MNRAS, 394, 929
Cacciato M., van den Bosch F. C., More S., Mo H., Yang X., 2013, MNRAS, 430, 767
Castorina E., Sefusatti E., Sheth R. K., Villaescusa-Navarro F., Viel M., 2014, J. Cosmology Astropart. Phys., 2, 049
Castorina E., Carbone C., Bel J., Sefusatti E., Dolag K., 2015, J. Cosmology Astropart. Phys., 7, 043
Chang C. et al., 2013, MNRAS, 434, 2121
Chaves-Montero J., Angulo R. E., Schaye J., Schaller M., Crain R. A., Furlong M., Theuns T., 2016, MNRAS, 460, 3100
Choi A. et al., 2016, MNRAS, 463, 3737
Clampitt J., Jain B., 2015, MNRAS, 454, 3357
Coe D., Benítez N., Sánchez S. F., Jee M., Bouwens R., Ford H., 2006, AJ, 132, 926
Coil A. L. et al., 2011, ApJ, 741, 8
Conroy C., Wechsler R. H., Kravtsov A. V., 2006, ApJ, 647, 201
Coupon J. et al., 2015, MNRAS, 449, 1352
Cunha C. E., Lima M., Oyaizu H., Frieman J., Lin H., 2009, MNRAS, 396, 2379
Cunha C. E., Huterer D., Busha M. T., Wechsler R. H., 2012, MNRAS, 423, 909
Cunha C. E., Huterer D., Lin H., Busha M. T., Wechsler R. H., 2014, MNRAS, 444, 129
Dalal N., White M., Bond J. R., Shirokov A., 2008, ApJ, 687, 12
Dark Energy Survey Collaboration et al., 2016, MNRAS, 460, 1270
Dawson K. S. et al., 2013, AJ, 145, 10
Dolag K., Borgani S., Murante G., Springel V., 2009, MNRAS, 399, 497
Dvali G., Gabadadze G., Porrati M., 2000, Phys. Lett. B, 485, 208
Eisenstein D. J. et al., 2011, AJ, 142, 72
Erben T. et al., 2009, A&A, 493, 1197
Erben T. et al., 2013, MNRAS, 433, 2545
Fenech Conti I., Herbonnet R., Hoekstra H., Merten J., Miller L., Viola M., 2016, MNRAS, preprint (arXiv:1606.05337)
Fontanot F., Villaescusa-Navarro F., Bianchi D., Viel M., 2015, MNRAS, 447, 3361
Fukugita M., Ichikawa T., Gunn J. E., Doi M., Shimasaku K., Schneider D. P., 1996, AJ, 111, 1748
Gao L., White S. D. M., 2007, MNRAS, 377, L5
Gao L., Springel V., White S. D. M., 2005, MNRAS, 363, L66
Genel S. et al., 2014, MNRAS, 445, 175
Giannantonio T. et al., 2016, MNRAS, 456, 3213
Gunn J. E. et al., 1998, AJ, 116, 3040
Gunn J. E. et al., 2006, AJ, 131, 2332
Guo H., Zehavi I., Zheng Z., 2012, ApJ, 756, 127
Hartlap J., Simon P., Schneider P., 2007, A&A, 464, 399
Hearin A. P., 2015, MNRAS, 451, L45
Hearin A. P., Watson D. F., Becker M. R., Reyes R., Berlind A. A., Zentner A. R., 2014, MNRAS, 444, 729
Hearin A. et al., 2016, AAS, preprint (arXiv:1606.04106)
Heymans C. et al., 2012, MNRAS, 427, 146
Heymans C. et al., 2013, MNRAS, 432, 2433
Hilbert S., Hartlap J., Schneider P., 2011, A&A, 536, A85
Hilbert S., Xu D., Schneider P., Springel V., Vogelsberger M., Hernquist L., 2016, MNRAS, preprint (arXiv:1606.03216)
Hildebrandt H. et al., 2012, MNRAS, 421, 2355
Hildebrandt H. et al., 2017, MNRAS, 465, 1454
Hinshaw G. et al., 2013, ApJS, 208, 19
Hirata C. M. et al., 2004, MNRAS, 353, 529
Ichiki K., Takada M., 2012, Phys. Rev. D, 85, 063521
Jee M. J., Tyson J. A., Schneider M. D., Wittman D., Schmidt S., Hilbert S., 2013, ApJ, 765, 74
Jeong D., Komatsu E., Jain B., 2009, Phys. Rev. D, 80, 123527
Jing Y. P., 1998, ApJ, 503, L9
Joudaki S. et al., 2017, MNRAS, 465, 2033
Joyce A., Lombriser L., Schmidt F., 2016, Annu. Rev. Nucl. Part. Phys., 66, 95
Kitaura F.-S., Yepes G., Prada F., 2014, MNRAS, 439, L21
Klypin A., Yepes G., Gottlöber S., Prada F., Heß S., 2016, MNRAS, 457, 4340
Kneib J.-P. et al., 2003, ApJ, 598, 804
Komatsu E. et al., 2009, ApJS, 180, 330
Kravtsov A. V., Berlind A. A., Wechsler R. H., Klypin A. A., Gottlöber S., Allgood B., Primack J. R., 2004, ApJ, 609, 35
Kuijken K. et al., 2015, MNRAS, 454, 3500
Kwan J., Heitmann K., Habib S., Padmanabhan N., Lawrence E., Finkel H., Frontiere N., Pope A., 2015, ApJ, 810, 35
Lacerna I., Padilla N., 2011, MNRAS, 412, 1283
Lam T. Y., Nishimichi T., Schmidt F., Takada M., 2012, Phys. Rev. Lett., 109, 051301
Laureijs R. et al., 2011, preprint (arXiv:1110.3193)
Le Fèvre O. et al., 2004, A&A, 428, 1043

Leauthaud A., Tinker J., Behroozi P. S., Busha M. T., Wechsler R. H., 2011, ApJ, 738, 45

Leauthaud A. et al., 2012, ApJ, 744, 159

Leauthaud A. et al., 2016, MNRAS, 457, 4021

Lehmann B. V., Mao Y.-Y., Becker M. R., Skillman S. W., Wechsler R. H., 2017, ApJ, 834, 37

Lesgourgues J., Pastor S., 2006, Phys. Rep., 429, 307

Levi M. et al., 2013, preprint (arXiv:1308.0847)

Li Y., Mo H. J., Gao L., 2008, MNRAS, 389, 1419

Li B., Zhao G.-B., Teyssier R., Koyama K., 2012, JCAP, 1, 51

Li B., Zhao G.-B., Koyama K., 2013, J. Cosmology Astropart. Phys., 5, 23

Lima M., Cunha C. E., Oyaizu H., Frieman J., Lin H., Sheldon E. S., 2008, MNRAS, 390, 118

Lin Y.-T., Mandelbaum R., Huang Y.-H., Huang H.-J., Dalal N., Diemer B., Jian H.-Y., Kravtsov A., 2016, ApJ, 819, 119

Lombriser L., Schmidt F., Baldauf T., Mandelbaum R., Seljak U., Smith R. E., 2012, Phys. Rev. D, 85, 102001

LSST Science Collaboration et al., 2009, preprint (arXiv:0912.0201)

Macciò A. V., Dutton A. A., van den Bosch F. C., 2008, MNRAS, 391, 1940

MacCrann N., Zuntz J., Bridle S., Jain B., Becker M. R., 2015, MNRAS, 451, 2877

Mandelbaum R., Seljak U., Kauffmann G., Hirata C. M., Brinkmann J., 2006a, MNRAS, 368, 715

Mandelbaum R., Seljak U., Cool R. J., Blanton M., Hirata C. M., Brinkmann J., 2006b, MNRAS, 372, 758

Mandelbaum R. et al., 2008, MNRAS, 386, 781

Mandelbaum R. et al., 2011, MNRAS, 410, 844

Mandelbaum R., Slosar A., Baldauf T., Seljak U., Hirata C. M., Nakajima R., Reyes R., Smith R. E., 2013, MNRAS, 432, 1544

Mandelbaum R., Wang W., Zu Y., White S., Henriques B., More S., 2016, MNRAS, 457, 3200

Maraston C. et al., 2013, MNRAS, 435, 2764

Margoniner V. E., Wittman D. M., 2008, ApJ, 679, 31

Melchior P., Sutter P. M., Sheldon E. S., Krause E., Wandelt B. D., 2014, MNRAS, 440, 2922

Melchior P. et al., 2015, MNRAS, 449, 2219

Miller L. et al., 2013, MNRAS, 429, 2858

Miralda-Escude J., 1991, ApJ, 370, 1

Miyatake H., More S., Takada M., Spergel D. N., Mandelbaum R., Rykoff E. S., Rozo E., 2016, Phys. Rev. Lett., 116, 041301

More S., 2013, ApJ, 777, L26

More S., Kravtsov A. V., Dalal N., Gottlöber S., 2011, ApJS, 195, 4

More S., van den Bosch F. C., Cacciato M., More A., Mo H., Yang X., 2013, MNRAS, 430, 747

More S., Miyatake H., Mandelbaum R., Takada M., Spergel D. N., Brownstein J. R., Schneider D. P., 2015, ApJ, 806, 2

More S. et al., 2016, ApJ, 825, 39

Nakajima R., Mandelbaum R., Seljak U., Cohn J. D., Reyes R., Cool R., 2012, MNRAS, 420, 3240

Navarro J. F., Frenk C. S., White S. D. M., 1997, ApJ, 490, 493

Nelson D. et al., 2015, Astron. Comput., 13, 12

Newman J. A. et al., 2013, ApJS, 208, 5

Palanque-Delabrouille N. et al., 2015, J. Cosmology Astropart. Phys., 2, 045

Paranjape A., Kovač K., Hartley W. G., Pahwa I., 2015, MNRAS, 454, 3030

Peacock J. A., Smith R. E., 2000, MNRAS, 318, 1144

Planck Collaboration XIII, 2016, A&A, 594, A13

Planck Collaboration XVI, 2014, A&A, 571, A16

Planck Collaboration XXIV, 2016, A&A, 594, A24

Prada F., Klypin A. A., Cuesta A. J., Betancort-Rijo J. E., Primack J., 2012, MNRAS, 423, 3018

Reddick R. M., Wechsler R. H., Tinker J. L., Behroozi P. S., 2013, ApJ, 771, 30

Reddick R. M., Tinker J. L., Wechsler R. H., Lu Y., 2014, ApJ, 783, 118

Reid B. A., Seo H.-J., Leauthaud A., Tinker J. L., White M., 2014, MNRAS, 444, 476

Reid B. et al., 2016, MNRAS, 455, 1553

Reyes R., Mandelbaum R., Seljak U., Baldauf T., Gunn J. E., Lombriser L., Smith R. E., 2010, Nature, 464, 256

Reyes R., Mandelbaum R., Gunn J. E., Nakajima R., Seljak U., Hirata C. M., 2012, MNRAS, 425, 2610

Riebe K. et al., 2013, Astron. Nachr., 334, 691

Rodríguez-Torres S. A. et al., 2016, MNRAS, 460, 1173

Ross A. J. et al., 2012, MNRAS, 424, 564

Ross A. J. et al., 2017, MNRAS, 464, 1168

Rozo E., Rykoff E. S., 2014, ApJ, 783, 80

Rykoff E. S. et al., 2014, ApJ, 785, 104

Saito S., Takada M., Taruya A., 2008, Phys. Rev. Lett., 100, 191301

Saito S., Takada M., Taruya A., 2009, Phys. Rev. D, 80, 083528

Saito S., Takada M., Taruya A., 2011, Phys. Rev. D, 83, 043529

Saito S. et al., 2016, MNRAS, 460, 1457

Samushia L. et al., 2013, MNRAS, 429, 1514

Schmidt F., 2009, Phys. Rev. D, 80, 123003

Schmidt F., 2010, Phys. Rev. D, 81, 103002

Sheldon E. S. et al., 2004, AJ, 127, 2544

Sijacki D., Vogelsberger M., Genel S., Springel V., Torrey P., Snyder G. F., Nelson D., Hernquist L., 2015, MNRAS, 452, 575

Simet M., Mandelbaum R., 2015, MNRAS, 449, 1259

Simet M., McClintock T., Mandelbaum R., Rozo E., Rykoff E., Sheldon E., Wechsler R. H., 2017, MNRAS, 466, 3103

Spergel D. et al., 2013, preprint (arXiv:1305.5425)

Springel V., White S. D. M., Tormen G., Kauffmann G., 2001, MNRAS, 328, 726

Springel V., Di Matteo T., Hernquist L., 2005, ApJ, 620, L79

Takada M. et al., 2014, PASJ, 66, R1

The Dark Energy Survey Collaboration et al., 2016, Phys. Rev. D, 94, 022001

Tinker J., Kravtsov A. V., Klypin A., Abazajian K., Warren M., Yepes G., Gottlöber S., Holz D. E., 2008, ApJ, 688, 709

Tinker J. L., Robertson B. E., Kravtsov A. V., Klypin A., Warren M. S., Yepes G., Gottlöber S., 2010, ApJ, 724, 878

Tinker J. L., Leauthaud A., Bundy K., George M. R., Behroozi P., Massey R., Rhodes J., Wechsler R. H., 2013, ApJ, 778, 93

van Daalen M. P., Schaye J., McCarthy I. G., Booth C. M., Dalla Vecchia C., 2014, MNRAS, 440, 2997

van den Bosch F. C., More S., Cacciato M., Mo H., Yang X., 2013, MNRAS, 430, 725

Velander M. et al., 2014, MNRAS, 437, 2111

Velliscig M., van Daalen M. P., Schaye J., McCarthy I. G., Cacciato M., Le Brun A. M. C., Dalla Vecchia C., 2014, MNRAS, 442, 2641

Villaescusa-Navarro F., Marulli F., Viel M., Branchini E., Castorina E., Sefusatti E., Saito S., 2014, J. Cosmology Astropart. Phys., 3, 11

Viola M. et al., 2015, MNRAS, 452, 3529

Vogelsberger M. et al., 2014a, MNRAS, 444, 1518

Vogelsberger M. et al., 2014b, Nature, 509, 177

Wechsler R. H., Zentner A. R., Bullock J. S., Kravtsov A. V., Allgood B., 2006, ApJ, 652, 71

Weinberger R. et al., 2017, MNRAS, 465, 3291

White M., Tinker J. L., McBride C. K., 2014, MNRAS, 437, 2594

Wilson G., Kaiser N., Luppino G. A., Cowie L. L., 2001, ApJ, 555, 572

Yoo J., Tinker J. L., Weinberg D. H., Zheng Z., Katz N., Davé R., 2006, ApJ, 652, 26

Zennaro M., Bel J., Villaescusa-Navarro F., Carbone C., Sefusatti E., Guzzo L., 2017, MNRAS, 466, 3244

Zentner A. R., 2007, Int. J. Mod. Phys. D, 16, 763

Zentner A. R., Hearin A. P., van den Bosch F. C., 2014, MNRAS, 443, 3044

Zentner A. R., Hearin A., van den Bosch F. C., Lange J. U., Villarreal A., 2016, MNRAS, preprint (arXiv:1606.07817)

Zhang P., Liguori M., Bean R., Dodelson S., 2007, Phys. Rev. Lett., 99, 141302

Zhao G.-B. et al., 2013, MNRAS, 436, 2038

Zheng Z. et al., 2005, ApJ, 633, 791

Zheng Z., Coil A. L., Zehavi I., 2007, ApJ, 667, 760

Zu Y., Mandelbaum R., 2015, MNRAS, 454, 1161

Zu Y., Weinberg D. H., Jennings E., Li B., Wyman M., 2014, MNRAS, 445, 1885

APPENDIX A: CROSS-CHECKS AND WEAK-LENSING SYSTEMATIC TESTS

A1 On the computation of a boost correction factor to account for physically associated galaxies

As described in Section 2.2.4, we use photo-z cuts to select background source galaxies ($z_S > z_L$). However, because photo-z estimates are far from perfect, our 'background' sample may contain a number of galaxies that are either actually in the foreground ($z_S < z_L$) or that are physically associated with the lens sample ($z_S = z_L$). Because foreground and physically associated galaxies are unlensed, the inclusion of these galaxies will cause $\Delta\Sigma$ to be underestimated ('dilution' effect). The exact magnitude of this effect will depend on the quality of the photo-zs, as well as the details of the lens–source separation cuts.

A boost correction factor is sometimes applied in order to account for the dilution of the signal by physically associated sources (e.g. Kneib et al. 2003; Hirata et al. 2004; Sheldon et al. 2004; Mandelbaum et al. 2006b). This correction factor is usually computed by comparing the weighted number density of source galaxies for the lens sample to the weighted number density of source galaxies around random points:

$$C(r) = \frac{N_{\mathrm{rand}}}{N_{\mathrm{lens}}} \frac{\sum_{\mathrm{lens}} w_{\mathrm{lens}}}{\sum_{\mathrm{rand}} w_{\mathrm{rand}}}. \tag{A1}$$

However, a key assumption underlying this procedure is that physically associated galaxies are the dominant contribution to $C(r)$. In practice, other effects may also modify the number density of source galaxies as a function of lens-centric distance such as magnification bias (Mandelbaum et al. 2006b), obscuration effects (Applegate et al. 2014; Melchior et al. 2015; Simet & Mandelbaum 2015), and local galaxy dependent quality cuts (Applegate et al. 2014; Melchior et al. 2015). The latter is particularly pernicious for the CFHTLenS and CS82 catalogues due to conservative deblending settings used by the *lens*fit shape measurement algorithm. Another effect that has been less discussed, is the availability of a photometric redshift. Indeed, in addition to shape measurements, photometry measurements may also be more likely to fail in high-density regions which would impact the radial density

profile of galaxies with reliable photo-zs. If these effects are not taken into account, boost-factors will be misestimated.

To illustrate the impact of lensing and photo-z quality cuts on the radial source density profile, we compute the number of source galaxies in the CS82 catalogue as a function of lens-centric distance after applying each of the following cuts in order:

(i) remove objects classified as stars by *lens*fit (FITCLASS =1) as well as objects in masked regions;

(ii) remove blended objects (FITCLASS =−2);

(iii) apply a FITCLASS =0 cut. This cut removes objects which have a bad fit, or for which the chi-squared exceeds a critical value;

(iv) select galaxies with a non-zero lensing weight ($w > 0$);

(v) select galaxies with $z_{\mathrm{phot}} > 0$ and ODDS >0.5.

Fig. A1 displays the results of this exercise and demonstrates that lensing and photo-z quality cuts have a non-trivial impact on the radial density profile of source galaxies out to scales of at least 1 h^{-1} Mpc. At first glance, it may tempting to think that Fig. A1 provides a straightforward characterization of the impact of each of these cuts. However, it is important to remember that each cut removes a set of legitimate background galaxies, but also modifies the number of physically associated pairs (there is no reason this number should remain constant after each cut) – and disentangling these two effects is non-trivial. The best approach so far to this problem has been to characterize the combined effects of obscuration and of the lensing quality cuts by computing the recovery rate of fake galaxies inserted into real images (Melchior et al. 2015). However, in addition to these effects, photo-z quality cuts may also have a non-trivial local galaxy dependance. This effect has been less discussed so far but warrants further attention.

Given these difficulties, we do not apply boost correction factors in this paper. Instead, we adopt a more empirical approach and check that our lensing signal is robust to various lens–source separation cuts. Indeed, if our signal is affected by a dilution effect, then we should find that the amplitude of the lensing signal on small scales increases as we implement more conservative lens–source separation cuts. In the following section, we demonstrate that we do not observe this effect – suggesting that our lens–source separation cuts are stringent enough that our lensing signals do not suffer from a dilution caused by physically associated galaxies. However, it is
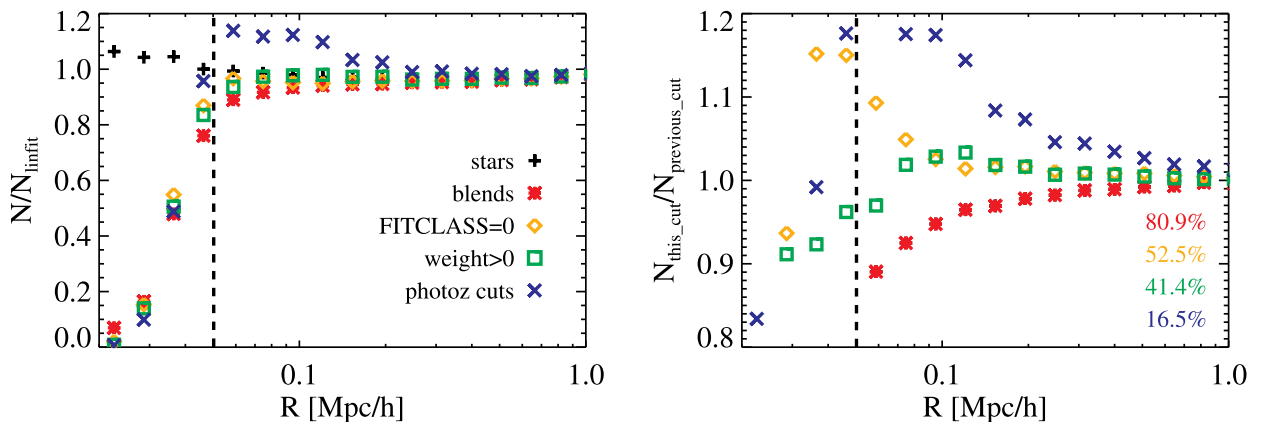

Figure A1. Number of source galaxies in the CS82 catalogue as a function of lens-centric distance after applying each of our lensing photo-z quality cuts. In this exercise, all source galaxies are artificially placed at $z = 0.8$. Left: number of objects in the source catalogue after each cut, divided by the expected value from a linear fit to the number of objects at $r > 1\ h^{-1}$ Mpc. The dashed vertical line indicates the minimum radial scale of our lensing measurement. Right: number of objects in the source catalogue divided by the number from the previous cut. Numbers in the right-hand panel indicate the fraction of galaxies that remain in the catalogue after each cut compared to the initial number. Lensing and photo-z quality cuts impact the radial source density profile out to scales of at least 1 h^{-1} Mpc.
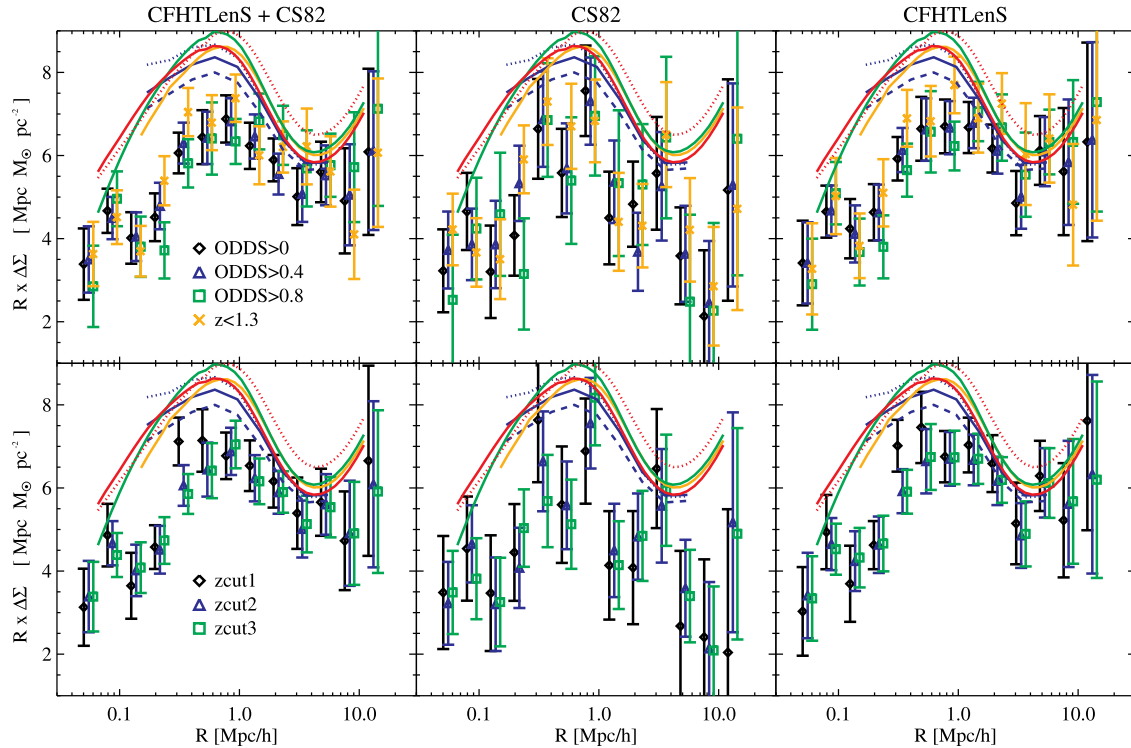
Figure A2. Tests for systematic effects associated with photometric redshifts. Left-hand panels: combined CS82 and CFHTLenS lensing signal. Middle panels: CS82 lensing signal. Right-hand panels: CFHTLenS lensing signal. Upper panels show the lensing signal computed for several different cuts on the ODDS parameter and when the source sample is restricted to $z_S < 1.3$. We do not display the results for $z_S > 1.3$ simply because only a small fraction of the source sample lies at $z_S > 1.3$ and the signal becomes too noisy to make a useful comparison. Lower panels show the lensing signal computed for three different lens–source separation cuts. As described in Appendix A2, ZCUT1 is a more conservative choice than ZCUT3 for selecting background galaxies. No statistically significant systematic trends are found for any of these tests. Lines represent model predictions using the same colour scheme as in Fig. 7. The CFHTLenS measurements appear to be more consistent with the model predictions at $r > 2 \ h^{-1}$ Mpc than CS82. However, as argued in Section 3.2, there is significant field-to-field variance on these scales which means that the combined CS82+CFHTLenS measurement (left-hand panels) should be more robust than either measurement alone.

clear that these effects warrant closer scrutiny using simulations such as presented by Melchior et al. (2015).

A2 Photometric redshifts

In this section, we present a series of tests to verify that our lensing signals are robust to a variety of different photometric redshift cuts. No statistically significant systematic trends are found for any of the tests that we have implemented.

First, we show that our lensing signal is robust with respect to BPZ ODDS parameter cuts. Fig. A2 presents the CMASS lensing signal computed for three different odds cuts (ODDS>0, ODDS>0.4, and ODDS>0.8). The fact that the amplitude of the signal is insensitive to this ODDS cut suggests that our signal is relatively robust to systematic errors due to catastrophic outliers.

Secondly, Hildebrandt et al. (2012) and Benjamin et al. (2013) caution that the quality of the CFHTLenS photometric redshifts degrade at $z_S > 1.3$. Our fiducial source catalogue does not include a high-redshift cut. To test if this choice impacts our results, we compute the lensing signal using only source galaxies with $z_S < 1.3$ and show the results in Fig. A2. We find no statistically significant shift in the signal when we enforce a source redshift cut at $z_S < 1.3$. A similar test with consistent results for CFHTLenS is presented in fig. C2 of Coupon et al. (2015).

Thirdly, we test if our results are robust with respect to the lens–source separation cuts. We consider three different schemes for

isolating background galaxies:

   (i) ZCUT1 : $z_S > z_L + 0.1$ and $z_S > z_L + \sigma_{95}$;
   (ii) ZCUT2 : $z_S > z_L + 0.1$ and $z_S > z_L + \sigma_{95}/2.0$;
   (iii) ZCUT3 : $z_S > z_L + 0.1$.

Here, ZCUT1 is a more conservative choice than ZCUT3. Our fiducial lens–source separation cut is ZCUT2. We compute the CMASS lensing signal using each of these three lens–source separation schemes and display the results in Fig. A2. The amplitude of our lensing signal does not vary when we enforce a more stringent lens–source separation scheme which suggests that our lensing signals do not suffer from a dilution caused by physically associated galaxies.

Finally, we use the combined spectroscopic redshift catalogue described in Section 2.2.3 to estimate the level of photo-z bias in $\Delta\Sigma$ for CS82. To correct for spectroscopic incompleteness and to ensure that the spectroscopic sample has the same distribution as our source sample, we use the weighting scheme described in Hildebrandt et al. (2017) which follow ideas originally outlined by Lima et al. (2008). This method determines the density in five-dimensional magnitude space of spectroscopic objects as well as objects in the lensing catalogue via a k-nearest neighbour estimate. The ratio of the densities at the position of each spectroscopic object is then used as a weight for this particular object. There are two main requirements for this method which are: (a) the spectroscopic catalogue must cover the whole extent of the lensing catalogue in magnitude space and (b) the mapping from magnitudes to redshifts
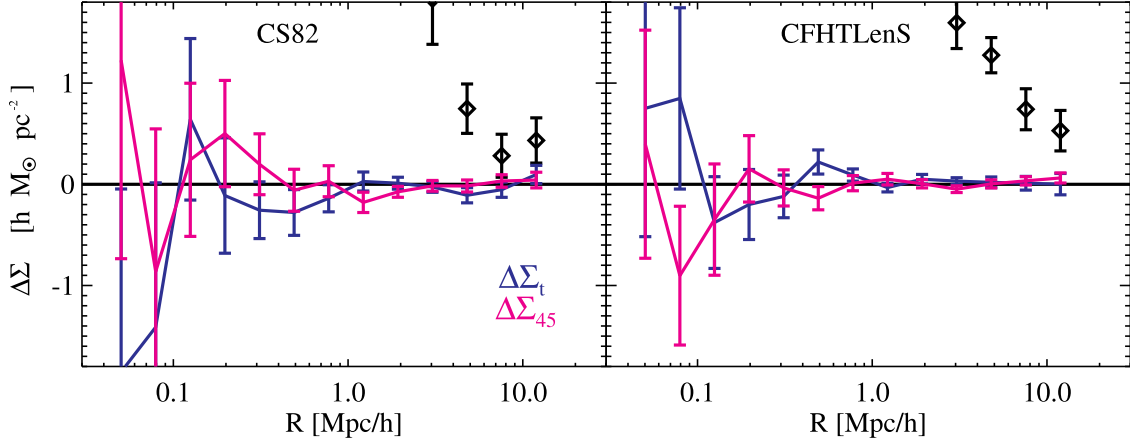
Figure A3. Stacked lensing signal around random points for CS82 (left) and CFHTLenS (right). Errors are computed via bootstrap. Black diamonds show the stacked lensing signal for CMASS galaxies. No statistically significant systematic shear patterns are detected around random points for either $\Delta\Sigma_t$ or $\Delta\Sigma_{45}$. The signal around random points becomes highly correlated on large-scales due to correlated shape noise.

must be unique. In our case, the first condition is satisfied. Even before re-weighting, the distribution of spec-z objects in magnitude space is very similar to the distribution of our source sample. Hence, the weights are rather small and only a mild re-weighting is necessary. The second requirement, however, is more difficult to quantify (see Lima et al. 2008; Cunha et al. 2009, 2012, 2014). However, given that we are using mostly objects with $i < 24$, which do not extend to very high redshifts, strong degeneracies are not expected.

We now outline our procedure to estimate the bias on $\Delta\Sigma$ arising from photo-zs by using our re-weighted spectroscopic sample (Mandelbaum et al. 2008; Nakajima et al. 2012). Let $\Delta\Sigma_P$ represent the (possibly biased) value of $\Delta\Sigma$ measured with photo-zs, and let $\Delta\Sigma_T$ represent the true value of $\Delta\Sigma$. Likewise, let $\Sigma_{crit,P}$ represent the value computed from photo-zs and $\Sigma_{crit,T}$ represent the true value of Σ_{crit}. The true value of the gravitational shear is simply:

$$\gamma_T = \Delta\Sigma_T/\Sigma_{crit,T}. \tag{A2}$$

If a source is at $z_S < z_L$, then $\gamma_T = 0$ (this accounts for the dilution effect by sources that scatter above z_L but which are actually located at lower redshifts than z_L). By combining equation (A2) with equation (4), we can form as estimate of $f_{bias} = \Delta\Sigma_T/\Delta\Sigma_P$ via:

$$f_{bias}^{-1} = \frac{\sum_{i=1}^{N_S} w_{spec,i} \left(\Sigma_{crit,P,i}/\Sigma_{crit,T,i}\right)}{\sum_{i=1}^{N_S} w_{spec,i}}, \tag{A3}$$

where the sum is performed over all source galaxies with spectroscopic redshifts and where the weight w_{spec} is analogous to w_{ds} but include the additional spectroscopic redshift weight described previously. When computing equation (A3) we randomly draw redshifts from our lens sample. Via this procedure, we find $f_{bias} = 0.97$ which suggests that biases due to photo-zs are at the 3 per cent level and are not a concern for this work. This estimate includes the dilution of the signal by source galaxies with $z_S^{spec} < z_L$ but $z_S^{phot} > z_L$.

A3 Signal around random points

As a test for systematic effects, we also compute the stacked lensing signal around a set of random points drawn from the same redshift distribution as our CMASS lens sample. For each of the two surveys, the density of random points is set to 100 times the density of the CMASS sample and errors on the signal around random points

are computed via bootstrap. The result is presented in Fig. A3. No statistically significant systematic shear patterns are detected around random points for either $\Delta\Sigma_t$ or $\Delta\Sigma_{45}$. We note that with this density of random points, the signal around random points becomes highly correlated on large scales due to correlated shape noise.

A4 Fibre collisions and redshift failures

As discussed in Section 2.1, a small number of galaxies from the CMASS target catalogue do not have a spectroscopic redshift because of fibre-collision effects and redshift measurement failures. We test four different schemes designed to account for these missing galaxies:

(i) WHT: the nearest neighbour based weighting scheme adopted in Anderson et al. (2012). In this approach, only galaxies that have a measured spectroscopic redshift are used when computing the lensing signal. Galaxies have a weight equal to $w_{tot} = w_{rf} + w_{fc} - 1$.

(ii) NN: galaxies that do not have a redshift are assigned the same redshift as their nearest neighbour (z_{NN}). In contrast with the previous method, galaxies that do not have a spectroscopic redshift *are* used when computing the lensing signal (with a redshift set to z_{NN}).

(iii) ZPHOT: CMASS galaxies that do not have a spectroscopic redshift are assigned a photo-z using the CFHTLenS and CS82 photo-z catalogues.

(iv) DISCARD: galaxies that do not have a spectroscopic redshift are removed from the catalogue. No additional weighting scheme is applied.

Fig. A4 demonstrates that the measured lensing does not depend strongly on the correction scheme for galaxies that do not have a spectroscopic redshift. The right-hand panel of Fig. A4 shows the impact of ignoring this effect altogether (the DISCARD scheme). The impact of missing redshifts from fibre collisions and redshift failures is small, but ignoring this effect altogether may lead to a small underestimate of the CMASS lensing signal because fibre collisions tend to occur in high-density regions (see discussion in Reid et al. 2014). For our fiducial signal, we adopt the nearest neighbour based weighting scheme (WHT).
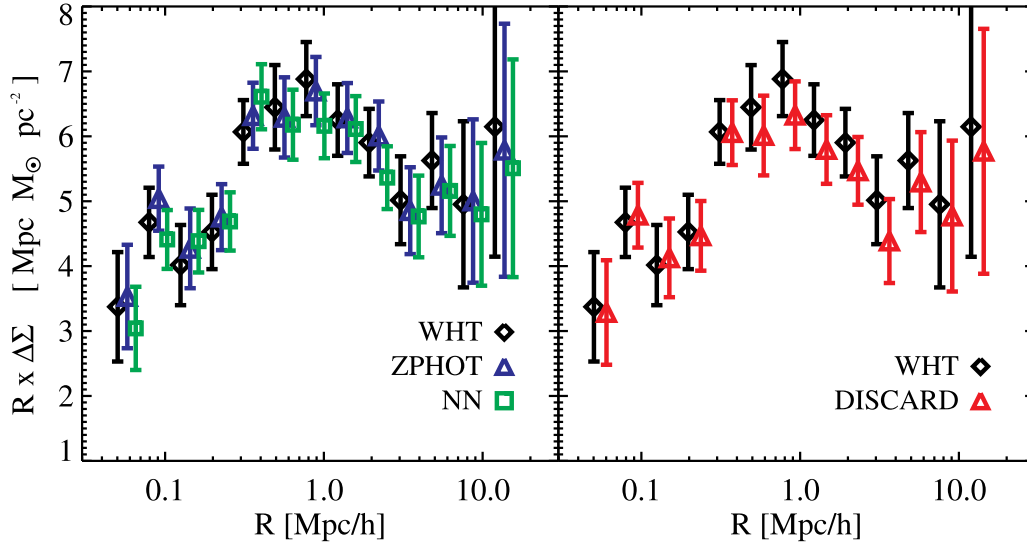
Figure A4. Left: lensing signal computed using three different methods to account for CMASS galaxies with missing spectroscopic redshifts. All three schemes yield similar lensing signals. Right: impact of ignoring objects with missing redshifts (DISCARD, red triangles) compared to our fiducial nearest neighbour based weighting scheme (WHT, black triangles). The red data points are systematically lower than the black data points suggesting that ignoring this effect altogether may lead to a small underestimate of the CMASS lensing signal because fibre collisions tend to occur in high-density regions (Reid et al. 2014).

A5 Weighting of the lensing signal

By examining equation (4), we see that not all lens galaxies will contribute an equal weight to $\Delta\Sigma$ (also see Nakajima et al. 2012; Mandelbaum et al. 2013; Simet et al. 2017). To highlight this, let us consider a single lens, i, and adopt the notations:

$$\Delta\Sigma_i = \frac{\sum_{j=1}^{N_S} w_{\text{ds},ij} \times \gamma_{\text{t},ij} \times \Sigma_{\text{crit},ij}}{\sum_{j=1}^{N_S} w_{\text{ds},ij}} \tag{A4}$$

$$w_{\text{lens,i}} = \sum_{j=1}^{N_S} w_{\text{ds},ij}. \tag{A5}$$

Using this notation, equation (4) can be rewritten as

$$\Delta\Sigma = \frac{\sum_{i=1}^{N_L} w_{\text{lens,i}} \times \Delta\Sigma_i}{\sum_{i=1}^{N_L} w_{\text{lens,i}}}. \tag{A6}$$

This is simply stating that in each radial bin, each lens is contributing to $\Delta\Sigma$ with a weight given by $w_{\text{lens, i}}$. There are several reasons why $w_{\text{lens, i}}$ will differ from lens-to-lens:

(i) there is a simple geometric effect in which the number of source galaxies per bin is redshift dependent when the bin size is fixed in comoving (or physical) units;

(ii) lenses at higher redshifts will have fewer source galaxies behind them;

(iii) lenses at higher redshifts will have a lower lensing efficiency (this is the $\Sigma_{\text{crit}}^{-2}$ term in w_{ds});

(iv) sources at higher redshifts will have a larger shape measurement uncertainty (this is the w term in w_{ds});

(v) obscuration and deblending effects mean that we lose a certain fraction of source galaxies on small radial scales (see Fig. A1 and discussion in Simet & Mandelbaum 2015). Because we expect obscuration and deblending effects to be more important for the central galaxies of massive haloes, this could lead to both a radial and a halo mass dependence of $w_{\text{lens, i}}$ which would go in the direction of down-weighting the lensing signal from massive haloes on small radial scales.

Can we explain our results simply due to differences in the weight function for CMASS galaxies between lensing and clustering measurements? Because the lensing signal does not vary with redshift (see Fig. 5), effects (i)–(iv) should have no impact on the lensing signal and so the main effect that we are concerned about is effect (v). Simet et al. (2017) tackle the first four effects by computing an average per-lens weight that is applied directly to their models. However, this approach is more difficult to apply in the context of obscuration and deblending effects because it would require characterizing $w_{\text{lens, i}}$ as a function of halo mass. For this reason, we propose a simple empirical test that accounts for the first four effects and partially accounts for the fifth effect. Instead of stacking the lensing signal over all lens galaxies, we first compute $\Delta\Sigma_i$ individually for each CMASS lens. We then compute an unweighted version of $\Delta\Sigma$ by simply taking the average value of $\Delta\Sigma_i$ in each radial bin as

$$\Delta\Sigma_{\text{noweight}} = \frac{\sum_{i=1}^{N_L} \times \Delta\Sigma_i}{N_L}. \tag{A7}$$

In this stack, lenses are no longer weighted by $w_{\text{lens, i}}$. However, this procedure only partially accounts for obscurations because haloes will still be down-weighted if obscuration effects are so large that there are no source galaxies in a given radial bin. Also, this estimator will have an increased variance compared to the traditional procedure because each lens is put on an equal footing instead of stacking by inverse variance.

Fig. A5 compares our fiducial signal with the reweighted signal computed following the procedure above. We find no evidence for a difference between our fiducial signal and the reweighted signal confirming our initial proposition that effects (i)–(iv) do not impact our lensing signal, but also suggesting that effect (v) is not large enough to be of concern. Finally, we remark that clustering measurements also have a specific weight function (because clustering measures pairs of galaxies, see for example Mandelbaum et al. 2011). However, because the lensing is invariant with redshift, applying an extra redshift-dependent weight to put the lensing on the same footing as the clustering should also have no effect.
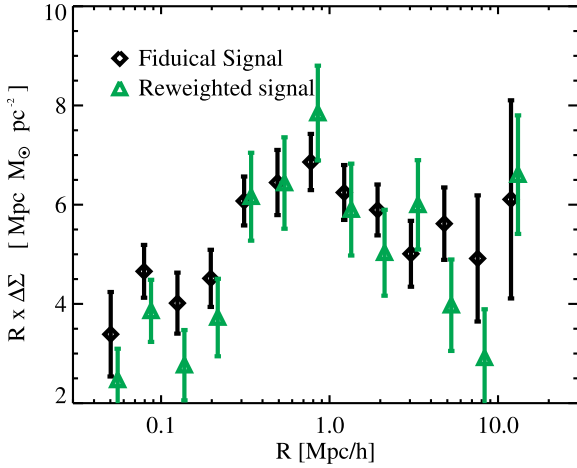
Figure A5. Fiducial signal (black triangles) compared to reweighted signal (green triangles).
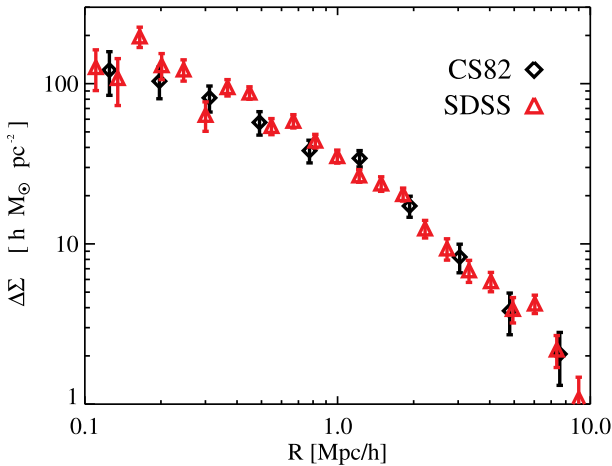

Figure A6. Comparison between the lensing signal computed from SDSS and the lensing signal computed from CS82 for redMaPPer clusters with $0.1 < z < 0.3$ and with $\lambda > 20$. The mean inverse-variance-weighted offset between the two signals is consistent with zero.

A6 Comparison with lensing from SDSS

Here, we perform a cross-check on our CS82 lensing catalogue by comparing with lensing from the SDSS catalogue of Reyes et al. (2012) with correction factors for photo-z errors as derived by Nakajima et al. (2012) and with the shear calibration described in Mandelbaum et al. (2013). We select a set of clusters from the redMaPPer cluster catalogue (v5.10, Rozo & Rykoff 2014; Rykoff et al. 2014) with $0.1 < z < 0.3$ and with $\lambda > 20$ where λ is the cluster richness and we compute the lensing signal around this sample for both CS82 and SDSS. Fig. A6 shows that the CS82 and SDSS lensing signals are in excellent agreement. This provides an overall sanity check on the CS82 lensing catalogue including the combined effects of shear calibration bias and the quality of the photoz-zs. The mean inverse-variance-weighted offset between the two signals for 0.1–$10 \ h^{-1}$ Mpc is (2.7 ± 7.0) per cent.

A7 Analytic HOD fit to projected correlation function

To construct Fig. 11, we fit a simple four parameter analytic HOD model to the w_p^{CMASS} measurements of Reid et al. (2014) assuming a redshift of $z = 0.55$. Our analytic HOD formalism is based on

code described in previous work (e.g. Leauthaud et al. 2011, 2012; Tinker et al. 2013) and assumes the halo mass function calibration of Tinker et al. (2008) and the halo bias calibration of Tinker et al. (2010). For consistency with our lensing measurements, we first convert the Reid et al. (2014) measurements to a cosmology with $\Omega_{\mathrm{m}} = 0.31$ following the methods outlined in More (2013). Our fit further assumes $\sigma_8 = 0.82$. Our HOD model assumes the following functional forms for the central and satellite occupation functions:

$$\langle N_{\mathrm{cen}} \rangle = \frac{1}{2} \left[1 + \mathrm{erf} \left(\frac{\log_{10}(M_{\mathrm{h}}) - \log_{10}(M_{\mathrm{min}})}{\sigma_{\mathrm{logM}}} \right) \right] \qquad \text{(A8)}$$

$$\langle N_{\mathrm{sat}} \rangle = \langle N_{\mathrm{cen}} \rangle \left(\frac{M_h}{M_1} \right)^{\alpha_{\mathrm{sat}}} , \qquad \text{(A9)}$$

where M_{h} is the halo mass defined as the mass enclosed by R_{200b}, the radius at which the mean interior density is equal to 200 times the mean matter density. The four parameters varied in our fit are: $\log_{10}(M_{\mathrm{min}})$, $\log_{10}(M_1)$, α_{sat}, σ_{logM}. We set a broad prior such that $3.2 \times 10^{-4} (h^{-1} \ \mathrm{Mpc})^{-3} < \bar{n} < 3.8 \times 10^{-4} (h^{-1} \ \mathrm{Mpc})^{-3}$. The best-fitting values from our fit are: $\log_{10}(M_{\mathrm{min}}) = 13.15 \pm 0.04$, $\log_{10}(M_1) = 14.26 \pm 0.05$, $\alpha_{\mathrm{sat}} = 1.07 \pm 0.09$, and $\sigma_{\mathrm{logM}} = 0.4540 \pm 0.06$.

[1] *Department of Astronomy and Astrophysics, University of California, Santa Cruz, 1156 High Street, Santa Cruz, CA 95064, USA*
[2] *Kavli IPMU (WPI), UTIAS, The University of Tokyo, Kashiwa, Chiba 277-8583, Japan*
[3] *Max-Planck-Institut für Astrophysik, Karl-Schwarzschild-Starße 1, D-85740 Garching bei München, Germany*
[4] *Exzellenzcluster Universe, Boltzmannstr. 2, D-85748 Garching, Germany*
[5] *Ludwig-Maximilians-Universität, Universitäts-Sternwarte, Scheinerstr. 1, D-81679 München, Germany*
[6] *Department of Physics, University of California, Berkeley, CA 94720, USA*
[7] *Department of Physics, McWilliams Center for Cosmology, Carnegie Mellon University, Pittsburgh, PA 15213, USA*
[8] *The Scottish Universities Physics Alliance, Institute for Astronomy, University of Edinburgh, Blackford Hill, Edinburgh EH9 3HJ, UK*
[9] *Astronomical Observatory of the University of Geneva, ch. d'Ecogia 16, CH-1290 Versoix, Switzerland*
[10] *Argelander-Institut für Astronomie, Auf dem Hügel 71, D-53121 Bonn, Germany*
[11] *Department of Physics, University of Oxford, Oxford OX1 3RH, UK*
[12] *Department of Physics and Astronomy, University College London, London, WC1E 6BT, UK*
[13] *Centro Brasileiro de Pesquisas Fisicas – Rua Dr. Xavier Sigaud 150, CEP 22290-180, Rio de Janeiro, RJ, Brazil*
[14] *Instituto de Física Teórica, (UAM/CSIC), Universidad Autónoma de Madrid, Cantoblanco, E-28049 Madrid, Spain*
[15] *Campus of International Excellence UAM+CSIC, Cantoblanco, E-28049 Madrid, Spain*
[16] *Departamento de Física Teórica M8, Universidad Autónoma de Madrid (UAM), Cantoblanco, E-28049 Madrid, Spain*
[17] *Laboratoire d'astrophysique (LASTRO), Ecole Polytechnique Fédérale de Lausanne (EPFL), Observatoire de Sauverny, CH-1290 Versoix, Switzerland*
[18] *INAF, Osservatorio Astronomico di Trieste, via Tiepolo 11, I-34131 Trieste, Italy*
[19] *INFN – National Institute for Nuclear Physics, Via Valerio 2, I-34127 Trieste, Italy*
[20] *Center for Computational Astrophysics, 160 5th Ave, New York, NY 10010, USA*